Kinetics of mouse and human muscle type nicotinic receptor channels

Dissertation zur Erlangung des
naturwissenschaftlichen Doktorgrades
der Julius-Maximilians-Universität Würzburg

vorgelegt von

Yunzhi Lu

Shanghai, China

Würzburg, 2019

Eingereicht am:

Mitglieder der Promotionskommission:

Vorsitzender: ……..

Gutachter: Prof. Dr. Manfred Heckmann

Gutachter: Prof. Dr. Christian Stigloher

Tag des Promotionskolloquiums:

Doktorurkunde ausgehändigt am:

Eidesstattliche Erklärungen nach §7 Abs. 2 Satz 3, 4, 5 der Promotionsordnung der Fakultät für Biologie

Eidesstattliche Erklärung

Hiermit erkläre ich an Eides statt, die Dissertation: „**Kinetik muriner und humaner nikotinischer Rezeptorkanäler vom Muskeltyp**“, eigenständig, d. h. insbesondere selbständig und ohne Hilfe eines kommerziellen Promotionsberaters, angefertigt und keine anderen, als die von mir angegebenen Quellen und Hilfsmittel verwendet zu haben.

Ich erkläre außerdem, dass die Dissertation weder in gleicher noch in ähnlicher Form bereits in einem anderen Prüfungsverfahren vorgelegen hat.

Weiterhin erkläre ich, dass bei allen Abbildungen und Texten bei denen die Verwertungsrechte (Copyright) nicht bei mir liegen, diese von den Rechtsinhabern eingeholt wurden und die Textstellen bzw. Abbildungen entsprechend den rechtlichen Vorgaben gekennzeichnet sind sowie bei Abbbildungen, die dem Internet entnommen wurden, der entsprechende Hypertextlink angegeben wurde.

Affidavit

I hereby declare that my thesis entitled: „**Kinetics of mouse and human muscle type nicotinic receptor channels**” is the result of my own work. I did not receive any help or support from commercial consultants. All sources and / or materials applied are listed and specified in the thesis.

Furthermore I verify that the thesis has not been submitted as part of another examination process neither in identical nor in similar form.

Besides I declare that if I do not hold the copyright for figures and paragraphs, I obtained it from the rights holder and that paragraphs and figures have been marked according to law or for figures taken from the internet the hyperlink has been added accordingly.

Würzburg, den_____

_____

Contents

1 Summary

Acetylcholine (ACh) mediates transmission at vertebrate neuromuscular junctions and many other synapses. The postsynaptic ACh receptors at neuromuscular junctions are of the nicotinic subtype (nAChRs). They are among the best studied receptor channels and often serve as models or receptor prototypes. Despite a wealth of information on muscle type nAChRs so far little is known about species specific functional differences. In this work, mouse and human adult muscle type nAChRs are investigated.

Cell attached recordings in the HEK293T heterologous expression system provided evidence that the ACh affinity of recombinant mouse and human adult muscle type nAChRs are different. To clarify this, I compared these receptors in outside-out patches employing a system for fast agonist application. Thus, the individual membrane patches with receptors can be exposed to various ligand concentrations. In response to 10 and 30 µM ACh normalized peak currents ($\hat{\imath}$) were significantly larger and current rise-time (t_r) shorter in human than in mouse receptors. Analyzing dose-response curves of $\hat{\imath}$ and t_r and fitting them with a two-step equivalent binding-site kinetic mechanism revealed a two-fold higher ACh association rate constant in human compared to mouse receptors. Furthermore, human nAChRs were blocked faster in outside-out patches by superfusion of 300 nM α-Bungarotoxin (α-Bgtx) than mouse nAChRs. Finally, human nAChRs in outside-out patches showed higher affinity at 3 µM ACh than chimeric receptors consisting of mouse α- and human β-, γ- and ε-subunits. The higher affinity of human than mouse receptors for ACh and α-Bgtx is thus at least in part due to sequence difference in their α-subunits.

1 Zusammenfassung

Acetylcholin (ACh) vermittelt Erregungsübertragung an neuromuskulären synaptischen Kontakten (neuromuscular junction, NMJ) von Wirbeltieren und vielen anderen Synapsen. Die postsynaptischen ACh-Rezeptoren an der NMJ sind vom nikotinischen Subtyp (nAChRs). Als Teil der am besten erforschten Kanalrezeptoren dienen sie oft als Modelle oder auch Prototypen für Rezeptoren. Trotz einer Fülle an Informationen über nAChRs des Muskeltyps ist bis heute recht wenig über artenspezifischen funktionellen Unterschiede bekannt. Diese Studie befasst sich daher mit der Untersuchung von nAChRs des Muskeltyps in erwachsenen Mäusen und Menschen.

Aufzeichnungen mit sogenannten Cell-attached Patches im heterologen Expressionssystem HEK293T-Zellen lieferten Beweise dafür, dass die ACh-Affinität von rekombinanten erwachsenen Maus- und menschlichen nAChRs vom Muskeltyp unterschiedlich sind. Um diesem nachzugehen, habe ich diese Rezeptoren in Outside-out Patches mit Hilfe eines schnellen Piezogetriebenen Applikationssystems verglichen. Dieses System bietet den Vorteil, dass einzelne Membran-Patches mit Rezeptoren unterschiedlichen Ligandenkonzentrationen ausgesetzt werden können. Als Reaktion auf 10 und 30 µM ACh waren die normalisierten Stromamplituden ($\hat{I}$) und Stromanstiegszeiten (t_r) der menschlichen Rezeptoren signifikant höher als die der Mausrezeptoren. Die Analyse der Dosis-Wirkungskurven von $\hat{I}$ und t_r sowie die Anpassung eines quantitativen zweistufigen kinetischen Modells mit zwei äquivalenten Bindestellen an die Datensätze zeigten eine zweifach höhere Assoziationsrate für ACh bei menschlichen Rezeptoren, verglichen mit der von Mausrezeptoren. Zudem wurden menschliche nAChRs in Outside-Out-Patches schneller als Mausrezeptoren durch Superfusion mit 300 nM α-Bungarotoxin (α-Bgtx) blockiert, was für eine höhere Affinität auch für α-Bgtx spricht. Schließlich wiesen die menschlichen nAChRs in Outside-Out-Patches bei 3 µM ACh eine höhere Affinität als chimäre Rezeptoren aus Maus α- und menschlichen β-, γ- and ε-Untereinheiten auf. Die höhere Affinität der menschlichen Rezeptoren zu ACh und α-Bgtx im Vergleich zu Mausrezeptoren basiert somit zumindest in Teilen auf Sequenzdifferenzen ihrer α-Einheitenen.

2 Introduction

2.1 Synaptic transmission

Synapses are structures that serve communication between neurons or between neurons and other target cells. The word "synapse", introduced by Sir Charles Scott Sherrington in 1897, comes from the Greek “synaptein” (“syn-” = “together” and “haptein” = “to clasp”). Two different modes for synaptic communication exist: electrical and chemical neurotransmissions. Unlike bi-directional transmission in electrical synapses, in chemical synapses a pre- and a postsynaptic part can be distinguished. This work focusses on chemical synapses, where presynaptic signals are transmitted through specific molecules (neurotransmitters) to receptors on the postsynaptic side. There are two principle types of neurotransmitter receptors: ionotropic and metabotropic receptors (Nicholls et al., 2000). Ionotropic receptors, which are investigated in this study, are ligand-gated ion channels (LGICs), consisting of ligand-binding sites and a gated pore. They interact with the neurotransmitters directly, causing fast synaptic transmission (in milliseconds) and modulating physical functions. Metabotropic receptors are slower, which mediate longer-lasting reactions (from many milliseconds to minutes) by engaging secondary messengers (Kandel, 2000; Hille, 2007).

Since the 20th century, electrophysiology has made it possible to study the electrical events at synapses. Pioneering work has been carried out at the vertebrate neuromuscular junction (NMJ), which revealed the physical process of synaptic signaling and the interaction between neurotransmitters and the postsynaptic nicotinic acetylcholine receptors (nAChRs) (del Castillo and Katz, 1956). Muscle type nAChRs are LGICs and bind acetylcholine (ACh). As a small molecule, ACh is a common neurotransmitter in nervous systems. nAChRs are the best studied ionotropic receptors.

The process of synaptic transmission at NMJs takes only milliseconds. When an action potential (AP) reaches the presynaptic terminal of a motor neuron, the membrane is depolarized, which initiates an influx of Ca^{2+} through voltage-dependent Ca^{2+} channels (Hodgkin, Huxley and Katz, 1949; Fatt and Katz, 1952). This triggers the fusion of ACh-containing synaptic vesicles (SVs) with the

presynaptic membrane and exocytosis of ACh. Neurotransmitters are released as quanta (Fatt and Katz, 1952). Each SV represents a quantal packet, containing around several thousand transmitter molecules. In the case of vertebrate NMJs, there are on average about 7000 ACh molecules in each quantum (Kuffler and Yoshikami, 1975). The number of vesicles in presynaptic terminals differs between species. SVs are released at specific sites called active zones (AZs). AZs of frog motor terminals are long and contain many SVs, while in mice only about 30 - 40 SVs are found per AZ (Slater, 2008; Nagwaney et al., 2009).

Released ACh diffuses in the synaptic cleft, which has a width of about 50 nm (Nicholls et al., 2000), and neurotransmitter reaches a high concentration with a maximum of up to ~ 1 mM ACh at vertebrate NMJs (Matthews-Bellinger and Salpeter, 1978). Only a fraction of the thousands of released molecules bind to postsynaptic nAChRs, while unbound ACh is either removed from the cleft by diffusion or hydrolyzed by the acetylcholinesterase (AChE) (Katz and Miledi, 1973a). Once ACh molecules bind to nAChRs, receptor channels open within 0.1 - 2 milliseconds, allowing Na^+-influx which leads to the depolarization of the postsynaptic membrane. A single vesicle or quantum causes a miniature end-plate potential (mEPP; Figure 1A, upper traces). When many vesicles are released simultaneously, an excitatory postsynaptic potential (EPSP) or end-plate potential (EPP) is formed (Figure 1A, lower traces) and the depolarization may reach a threshold on the postsynaptic side and an action potential may be formed. Propagation of the action potentials leads to muscle contraction.

Once ACh molecules dissociate from the receptor proteins, the receptor channels close, resulting in a return to equilibrium of the membrane potential. A sustained muscle contraction requires successive stimuli with an interval of about 10 ms. Fast synaptic transmission depends on rapid interactions between ACh and the receptors, which are inversely correlated with the receptor affinity, namely “low-affinity reactions”. The lower the affinity, the shorter the EPP time-course could be evoked at the NMJ (Eccles et al., 1942; Fatt and Katz, 1952; Dunant and Gisiger, 2017).

Muscle type nAChRs are localized opposite to presynaptic ACh-releasing AZs, on the crests of the membrane junctional folds (JFs) (Salpeter et al.,1984; Figure 1B).

At vertebrate NMJs, the number of postsynaptic receptors is much higher than the number of ACh molecules per quantum. Therefore, the number of open receptors depends on the number of SVs which are released and the accessibility of released-ACh to the receptor clusters at the JFs. Along with the receptor number, the affinity of the receptor also affects the receptor activation. The lower the affinity, the fewer receptors may open, generating a smaller synaptic response.

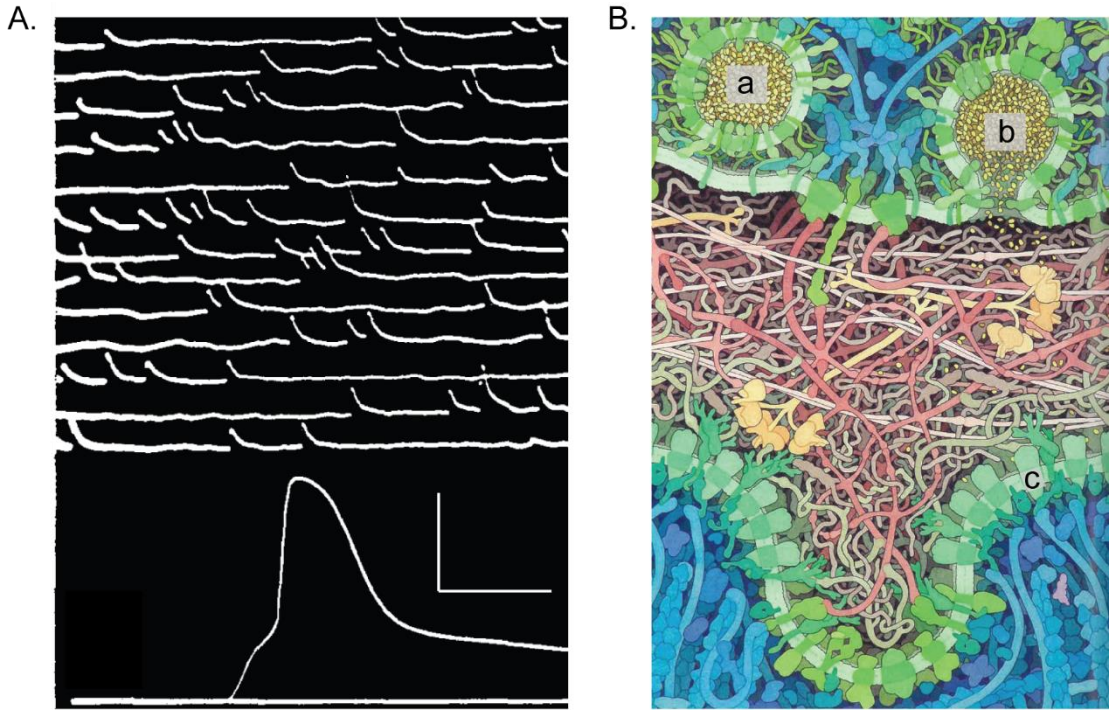

Figure 1. **Neuromuscular junctions.**

(A) Intracellular recording at a frog neuromuscular junction. In the upper half of the figure, a series of miniature end-plate potentials (mEPPs) is shown. Each mEPP is generated by the release of one ACh-containing presynaptic vesicle. In the lower part of the figure, an excitatory postsynaptic potential (EPSP) is demonstrated. An EPSP is stimulated when the presynaptic terminal evokes the nearly simultaneous release of ACh from many vesicles (modified from Fatt and Katz, 1952). The vertical and horizontal scale bars represent 3.6 mV and 47 ms for the upper half, and 50 mV and 2 ms for the lower part of the recording. **(B)** Artistic illustration of a frog neuromuscular junction, emphasizing the complex and dense interaction of macromolecules and ACh at a magnification of x 10^6: presynaptic vesicle release site (top), synaptic cleft (in between) and postsynaptic cell membrane (bottom). At this magnification, individual molecules such as ACh are about the size of a grain of salt and too small to be resolved. The postsynaptic membrane is extensively folded, forming junctional folds (JFs). One typical JF presents with receptor clusters. Two ACh-containing vesicles are shown. The one marked with an **a** is docked at the presynaptic cell membrane. The vesicle marked **b** is fusing with the cell membrane and releases ACh. On the postsynaptic side, a **c** is used to highlight one of the many muscle type nAChRs (modified from Goodsell, 2009).

2.2 Nicotinic acetylcholine receptors

Evolution Nicotinic acetylcholine receptors (nAChRs) originated many hundreds of millions of years ago and belong to the acetylcholine receptors family. Based on their relative affinities for various agonists, these receptors are classified into two major subtypes, namely, muscarinic and nicotinic AChRs. The later can be further subdivided into neuronal- and muscle-type receptors. They are generated by different combinations of 17 known subunits in vertebrate: *α* (*α*1 - *α*10), *β* (*β*1 - *β*4), *δ*, *ε* and *γ* (Le Novère et al., 2002). The phylogenetic database, which documents how the members of nAChRs relate to each other, has been continuously augmented (Tsunoyama and Gojobori, 1998; Le Novère et al., 2002; Pedersen et al., 2019). Today it is known that all subunits can be divided into four subsets: the neuronal subset (*α*2 - *α*6 and *β*2 - *β*4 subunits), the NMJ subset (*α*1-, *β*1-, *δ*-, *γ*- and *ε*-subunits), the *α*7 / *α*8 subset and the *α*9 / *α*10 subset (Figure 2). The earliest ancestral subunits of this family might have originated from the nervous system, *α*7 - *α*10 subunits (Le Novere and Changeux, 1995; Ortells and Lunt, 1995; Tsunoyama and Gojobori, 1998). All muscle type subunits were the products in the later stage of evolution (Lipovsek et al., 2012; Figure 2, magenta frames). Some of these subunits have been found of obvious functional differences among species (more details seen in Discussion 5.5), while the species functional differences of the other subunits have been little known.

Structure and conformational changes As the prototype for pentameric LGICs, nAChRs serves as a paradigm for studying other receptors. The first crystal structure of nAChRs came from the electric organs of *Torpedo* 30 years ago. *Torpedo* nAChRs have a high homology with those from vertebrate skeletal muscle (Numa et al., 1983; Changeux et al., 1998). Muscle type nAChRs are hetero-pentamers formed by four different subunits (*α*, *β*, *δ* and either *γ* or *ε*), more precisely named as *α*1- and *β*1-subunits. At the mammalian embryonic stage or in denervated muscles, the receptors are composed of subunits $\alpha_2\beta\gamma\delta$, named embryonic-type nAChRs. During the development, when muscle innervation proceeds, the *γ*-subunit gets gradually replaced by the *ε*-subunit, assembling adult type nAChRs ($\alpha_2\beta\varepsilon\delta$) (Mishina et al., 1986; Karlin and Akabas, 1995).

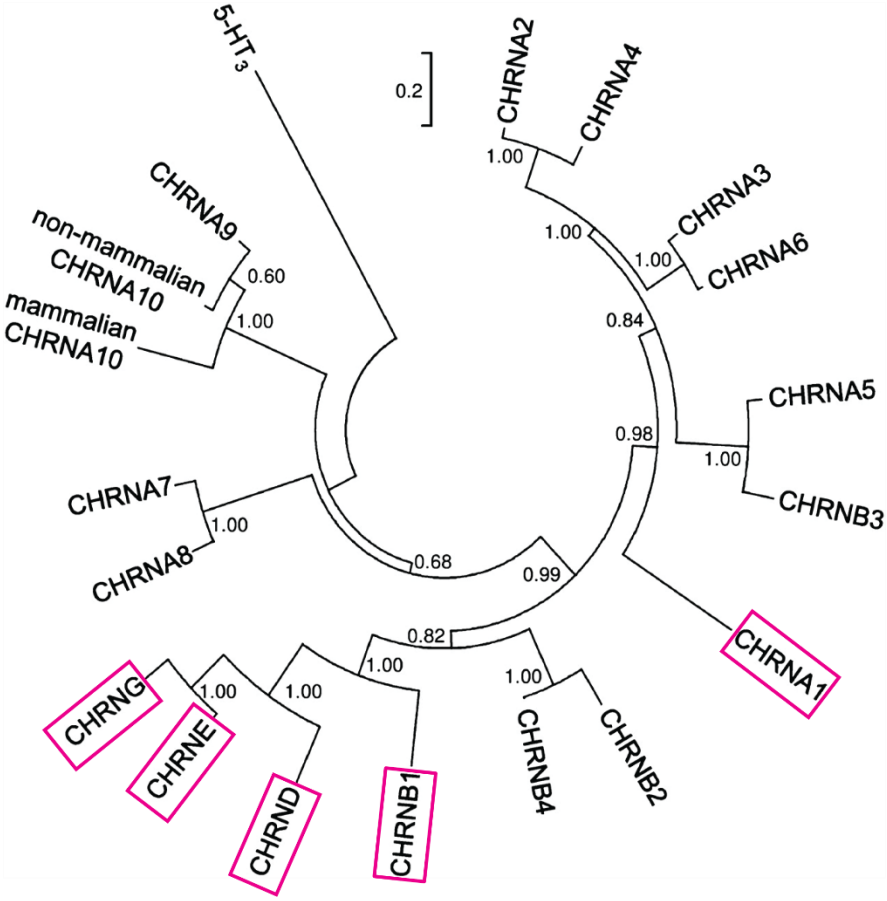

Figure 2. **Phylogenetic relationships among vertebrate nAChR subunits.**

The orthologs of each type of subunits are illustrated by the collapsed nodes. Each branch represents the same subunit of different organisms including mouse and human. Muscle-type subunits (*α*1, *β*1, *δ*, *ε* and *γ*) are highlighted in magenta frames, corresponding to A1, B1, D, E and G, separately. The subunits *α*2 - *α*10 and *β*2 - *β*4 are neuronal-type subunits. There is no obvious divergence detected between neuronal- and muscle-type subunits. *α*1-subunit diverged at an early stage of evolution with neuronal type subunits. Other muscle type subunits appeared later. The evolutionary sequence is: *β*1, *δ*, *ε* and *γ*. The numbers in the branches are the bootstrap values. The root is not given. The lengths of the branches are drawn to scale and proportional to their evolutionary distances (modified from Lipovsek et al., 2012).

When seen from the extracellular side, the five subunits form a “rosette” around a central axis perpendicularly (~ 65 Å in length) in the most plausible order of *α*, *γ* (or *ε*), *α*, *β* and *δ* clockwise (Karlin et al., 1983; Karlin, 1993; Figure 3A). Muscle type nAChRs contain two ligand-binding sites, located at the *α*-*γ* (or *ε*) and *α*-*δ* interfaces (Figure 3A, yellow circles). The *α*-subunits serve as the principal component, providing the main binding surface, while the adjacent subunits (*δ*, *γ* and *ε*) are the

complementary components (Blount and Merlie, 1989; Glazi and Changeux, 1994; Arias, 2000; Corringer, Novere and Changeux, 2000).

The whole receptor is composed of the extracellular domain (ECD), the transmembrane domain (TMD) and the intracellular domain (ICD). Each subunit has four transmembrane helices as shown in Figure 3B, with a long N-terminus (~ 200 amino acids) and a short C-terminus (~ 4 - 28 amino acids) extracellularly. All five subunits have highly similar amino acid sequences except the highly variable C-terminus (Hucho et al., 1996; Karlin, 2002; Unwin, 2005; Albuquerque et al., 2009). Various categories of ligand binding-sites exist in the ECD, such as those binding agonist and antagonists (Karlin, 1993; Karlin and Akabas, 1995; Arias, 2000; Corringer et al., 2012). The extracellular structure of the *α*-subunit is built around a curled β-sandwich core containing ten β strands. Loop A, B and C joining different β-sheets (Figure 3B) are functionally important for ligand-binding.

Numerous agonists can activate nAChRs, including acetylcholine, carbamylcholine, tetramethylammonium and epibatidine. As a natural neurotransmitter at nicotinic synapses, ACh is one of the most suitable agonists for identifying the pharmacological profile and pathogenic effects of nAChRs (Castillo and Katz, 1956; Ridley et al., 1984; Colquhoun and Ogden, 1988; Sine et al., 1995; Zhang et al.,1995; Ohno et al., 1996; Francis et al., 1999; Himmelheber et al., 2000; Nayak et al., 2016). The key residues in *α*-subunits required for ligand-binding are located in loops A, B and C, while loop C acts as the principal loop for ligand-binding (Brejc et al., 2001; Unwin, 2005; Dellisanti et al., 2007a). The complementary part, for example, the *γ*-subunit, contributes to loops D, E, F and G (Figure 4). These loops are involved in shaping the ligand-binding pockets and undergo various movements during channel-gating (Arias, 2000; Changeux and Taly, 2008; Unwin and Fujiyoshi, 2012). Through labelling, site-directed mutation and functional experiments, several critical residues in the hydrophobic ACh-binding pockets have been determined. These are located at the extracellular N-terminal domains of the respective subunits.

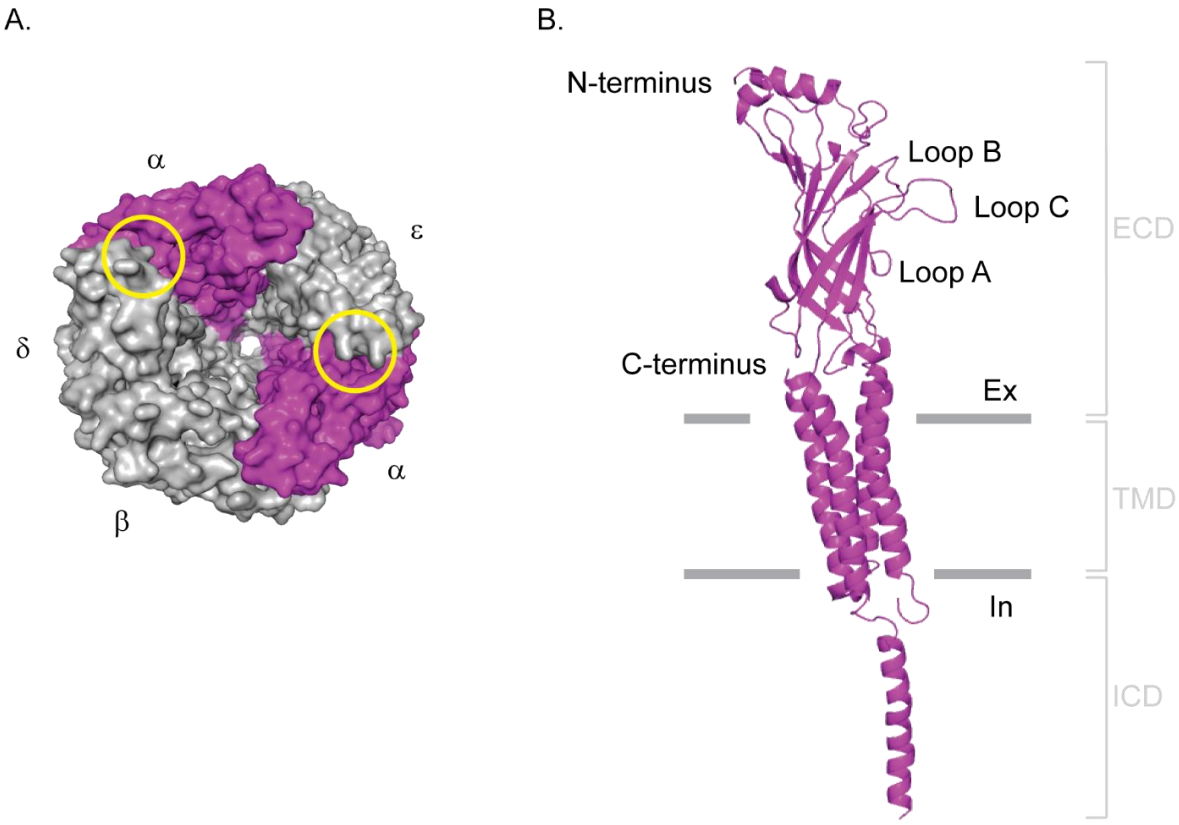

Figure 3. **Surface structure of a whole nAChR and the basic structure of a single *α*-subunit.**

(A) Top view of the nAChR seen from the synaptic cleft. The nAChR is a pentameric ion channel receptor. The ligand-binding sites at the *α*-*δ* and the *α*-*ε* interfaces, or in the case of the embryonic receptors at the *α*-*δ* and the *α*-*γ* interfaces, are labelled by yellow circles. The two equivalent *α*-subunits are colored in magenta. The *β*-, *δ*-, and *γ*- or *ε*-subunits are in grey. **(B)** Side view of a *α*-subunit. All the subunits share the same topology: the extracellular domain (ECD) on the top part, the helical-transmembrane domain (TMD) containing four transmembrane segments in the middle part and the large intracellular domain (ICD) on the bottom part. Loops A, B and C connect β-sheets in the ECD. The dimension of the bilayer lipid membrane is represented by grey bars (The structure is retrieved from the PDB database: 4AQ9).

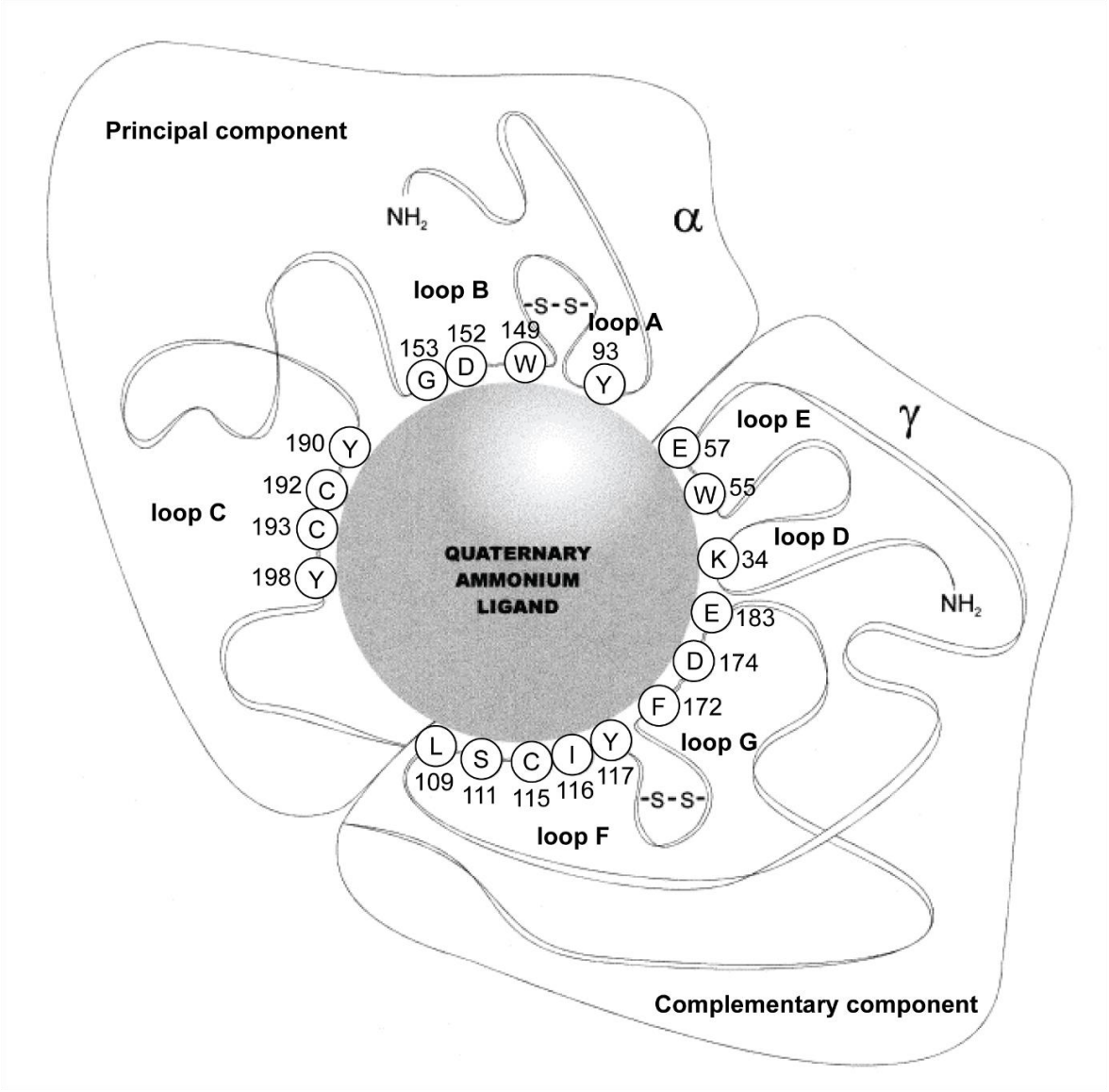

Figure 4. **Schematic representation of the ACh-binding site located at the *α-γ* interface in mouse nAChRs.**

The grey sphere represents ACh. Loops A, B and C belong to the principal component *α*-subunit, and loops D, E, F and G are in the complementary component *γ*-subunit. The key residues within each loop contributing to ACh-binding are displayed with one letter code in small spheres, along with their sequence numbers. For adult muscle type nAChRs, the ACh-binding sites are at the *α-δ* and the *α-ε* interfaces (modified from Arias, 2000).

Following agonist binding, the receptor conformation changes, mediating the central pore opening, which allows ions such as Na^+, K^+ and Ca^{2+} to pass through (Unwin, 2005). By using high-resolution electron microscopy together with X-ray diffraction studies of crystal structures, this whole process has been extensively investigated.

It is known that both the ligand-binding domains (LBDs) and TMDs contribute to the conformational change of the channel pore. In the resting state, the five transmembrane helices M2 are close to each other, lining an inner ring as a hydrophobic transmembrane pore. The interactions of the side chains in neighboring helices generate a “gate”, which blocks the pathway of ions through the pore. Other transmembrane helices (M1, M3 and M4) form an outer wall exposed to the lipid environment. It has also been identified that the conformational extension of the two *α*-subunits are different from other non-*α*-subunits. When agonist bound, it causes the inner β-sheets in the *α*-subunits to twist, which enlarges the distance between each M2 helix. The interacting residues in M2 helices rotate away from being exposed to the pore lumen and the gate opens. In addition, a local disturbance at each binding-site is initiated, that is the bending of loop C in the *α*-subunits towards the ligand-binding pocket in the open channel conformation (Unwin, 1995; Unwin et al., 2002; Miyazawa et al., 2003; Unwin and Fujiyoshi, 2012).

Competitive antagonist α-bungarotoxin (α-Bgtx), a typical α-neurotoxin present in the venom of the snake *Bungarus multicinctus*, can bind to muscle type nAChRs and block the action of agonists such as ACh. α-Bgtx is a long polypeptide neurotoxin with 74 amino acids, composed of one central globular core, three “finger-loops” and one C-terminal loop (Love and Stroud, 1986; Gentile et al., 1995; Zeng et al., 2001; Figure 5A). Once this polypeptide binds to the postsynaptic nAChRs at the NMJ, it causes paralysis of muscles and even lethality in severe cases (Dellisanti et al., 2007b; Ranawaka et al., 2013; Silva et al., 2017). Due to its high affinity and specificity for muscle type nAChRs, α-Bgtx has been widely used as a competitive antagonist in many studies to label and/or quantify nAChRs, as well as to detect channel blocking effects (Katz and Miledi, 1973b; Ishikawa et al., 1977; Franklin et al., 1980; Ishikawa et al., 1985; Askanas et al., 1987; Garcia-Borron et al., 1990; Vincent et al., 1997; Young et al., 2003).

Dellisanti and colleagues (2007) solved the structure of a complex comprising α-Bgtx with the ECD of a mouse nAChRs α-subunit at atomic-resolution level, where they found a specific bulky carbohydrate chain in the *α*-subunits of muscle type nAChRs, as well as several key amino acids for the toxin-receptor interaction (Dellisanti et al., 2007a; Figure 5B). In previous studies, loop C has been identified

as the most important structure for toxin-binding in the ECD (Arias, 2000; Dellisanti et al., 2007a, b). The interaction between loop C and this conserved carbohydrate chain, together with the cys-loop, plays an important role in the α-Bgtx binding and channel gating function. Once α-Bgtx binds, its loop I interacts with the carbohydrate chain, restricting the receptor conformational alteration. Also, α-Bgtx loop II can interact with the aromatic cage formed by the residues in *α*-subunits (positions at 93, 149, 190 and 198) and then prevents agonists from approaching the ligand-binding sites.

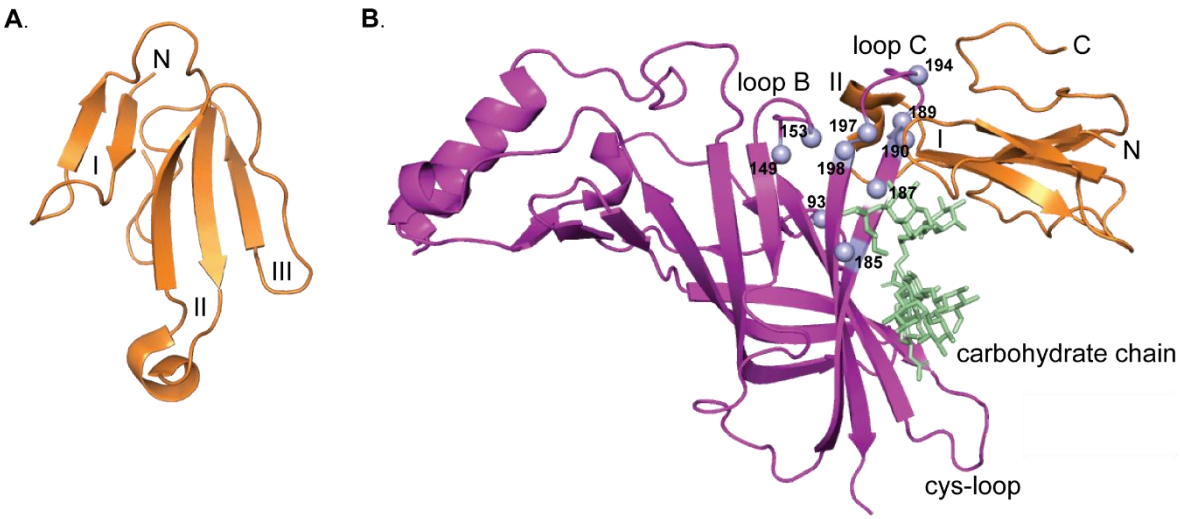

Figure 5. **α-bungarotoxin and the structure of mouse nAChR *α*-subunit ECD in complex with α-Bgtx.**

(A) Overall structure of α-Bgtx. The three finger loops (loop I, II and III) and the N-terminus are marked. Loop I, loop II and C-terminal loop form a hydrophobic region, which serves as the main part in α-Bgtx binding. Loop III is thought to be in touch with the neighbouring subunit, but only slightly. **(B)** Complex of α-Bgtx binding to the α-subunit ECD (retrieved from the PDB database: 2QC1). Loop I and II of α-Bgtx (orange) are wrapped around by loop C of the *α*-subunit. The carbohydrate chain (shown as stick diagram) in the *α*-subunit is positioned at the surface of the ECD, which links loop C and the cys-loop of the receptor, and also interacts with loop I in α-Bgtx. The interaction among these structures are very tight. Several key residues for toxin binding are marked as spheres in light blue (modified from Dellisanti et al., 2007a).

2.3 Kinetic mechanism of receptor reaction

With the development of the patch-clamp (Neher and Sakmann, 1976), as well as genetic and high-resolution protein structure techniques, refined kinetic schemes for nAChRs were suggested to describe the relationship between ligand-binding and

channel-gating in a quantitative manner. As early model for interpreting ACh receptor behavior was proposed by del Castillo and Katz (del Castillo and Katz, 1957; Figure 6). They pointed out that binding and gating are separate steps.

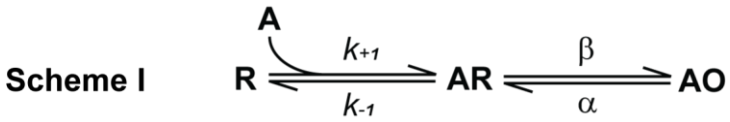

Figure 6. **Simple reaction mechanism for receptor channels.**

The mechanism of del Castillo and Katz (1957) is designated as Scheme I. Several points should be noted: (1) the binding sequence is represented as one step; (2) the forward association rate is proportional to the ligand concentration (k_{+1}·[A]); and (3) other possible states of the receptor, such as desensitized and/or blocked states, are not taken into account. R represents an un-liganded, inactive receptor; A is the agonist molecule; AR denotes an inactive intermediate state with agonist bound; and AO is an active open receptor. k_{+1} is the agonist association rate (unit: $M^{-1}\cdot s^{-1}$), k_{-1} is the agonist dissociation rate (unit: s^{-1}), and α and β stand for the channel closing and opening rate (unit: s^{-1}), respectively.

Benefiting from substantial investigations into the quantitative subunit compositions and the arrangement of muscle-derived nAChRs, the kinetic mechanism of receptor opening can be refined as a four-state model (Figure 7). The identification of the reaction process is limited by the low-resolution recording technique at the level of macroscopic response (Liu and Dilger, 1991).

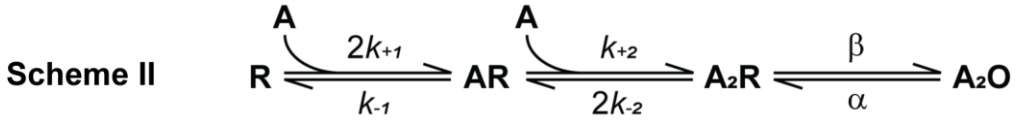

Figure 7. **Reaction scheme with two equivalent binding steps.**

Scheme II is a linear reaction scheme, in which only a double-liganded open state is defined and the two binding-sites of muscle type nAChRs are indistinguishable. R represents an inactive, un-liganded nAChR, A is the agonist ACh, AR and A_2R represent inactive receptor states with one or two agonists bound, respectively. A_2O is a double-liganded, active receptor. k_{+1} and k_{+2} are the association rate constants of each binding-site, k_{-1} and k_{-2} are the dissociation rate constants of each binding-site. For identical binding sites, there are $k_{+1} = k_{+2}$ and $k_{-1} = k_{-2}$.

The affinity for the agonists at two binding sites are assumed identical in Scheme II, in which the first binding step can happen either at the *α*-*γ* (or *ε*) or *α*-*δ* sites. The

current response can only be elicited, when both binding-sites are occupied by agonists and the receptor channels open. The postsynaptic current responses at the NMJ, caused by random fluctuations between activation and inactivation of many receptors, are observed at a macroscopic level (Katz and Miledi, 1970, 1971). In this case, the currents recorded in such situations are present as an average value (mean current, *I*).

In subsequent studies, a mono-liganded open state of nAChRs was observed (Karlin, 1967; Sine and Taylor, 1981). At the same time, the advance of noise analysis has made it possible to study currents flowing through ion receptor channels with single-channel resolution (Neher and Sakmann, 1976). Therefore, various types of channel opening events for muscle type nAChRs have been detected, and microscopic kinetic information of individual channels could be obtained (Colquhoun and Sakmann, 1981; Hallermann et al., 2005; Stock et al., 2014). Nowadays, the relationship between binding and gating steps is still under investigation. The effects produced by various agonists binding to nAChRs are distinct, which depend on the biochemical properties of the molecules and their physical functions. New schemes continue to emerge, which would doubtlessly provide new insights into the nAChRs binding-gating kinetics (more schemes seen in Discussion 5.2).

2.4 Motivation of the study

Proteins of the same family can be functionally different from one species to another. For example, haemoglobins of crocodiles and humans show interesting functional differences, which enable the crocodiles stay long time under the water to kill their prey by drowning (Komiyama et al., 1995). Crocodiles benefit from the bicarbonate binding effect of their haemoglobins (Kemp, 1995). Sequence alignment displays 110 out of 287 amino acids are different between Nile crocodile and human haemoglobins. Exchanging 12 amino acids was enough to introduce the bicarbonate binding ability into the human haemoglobin (Komiyama et al., 1995). Therefore, it is useful to study species specific functional differences of proteins.

Hence, I set out to study the difference of mouse and human nAChRs. As a standard animal model, mice obviously differ from humans, although they are remarkably

similar in many fundamental aspects. Our previous studies using single-channel recordings in cooperation with Dmitrij Ljaschenko (data unpublished) showed that at very low ACh concentration, long bursts of receptor openings were only detected in human receptors, but not in mouse nAChRs. This indicates a higher ACh affinity of human nAChRs than mouse receptors (see Results 4.1). It is of interest to further investigate their detailed difference.

The kinetics of mouse nAChRs activation have been extensively investigated through single channel measurements and those proposed kinetic models (Sine and Steinbach, 1986a; Chen et al., 1995; Zhang et al., 1995; Sine et al., 1995; Akk and Auerbach, 1996; Wang et al., 1997). Although high-resolution single-channel recordings can distinguish the various open states (mono-liganded and double-liganded openings) to some extent (Parzefall et al., 1998; Hallermann et al., 2005), there are some limitations to this method. For example, the opening rate estimated at high and low agonist concentrations are not consistent (Sine and Steinbach, 1986b, 1987), and it is impossible to directly elucidate the forward rates of channel activation. Also, these measurements are usually done in the cell-attached mode, where the recordings are made with a fixed drug concentration. This is not sufficient for explaining the channel behavior in situ. To avoid or compromise these problems, outside-out patches together with a fast application system (Brett et al., 1986; Franke et al.,1987; Maconochie and Knight, 1989; Dudel et al., 1990) were introduced as an alternative method. This achieves a rapid change of certain agonist concentrations to mimic synaptic transmission and enables to control the ion concentrations on both sides of the membrane. Besides, the macroscopic current measurements overcome the resolution limitation when detecting the single-channel opening (Franke et al., 1991b).

To my knowledge, no investigation has been done so far that compares the affinities of mouse and human nAChRs directly in excised patches with a fast agonist changing system. The aim of this study is to compare the ACh affinity and the affinity for α-Bgtx between mouse and human nAChRs, to describe the observations and to elucidate the structure-function relationships. This enables to better predict the functional responses of muscle nicotinic receptors based.

3 Materials and Methods

3.1 Chemicals and equipment

Eagle medium	Gibco, Life Technologies GmbH, Karlsruhe, Germany
NaCl	Merck Chemicals GmbH, Darmstadt, Germany
KCl	Sigma-Aldrich Co., St. Louis, USA
$CaCl_2$	Merck Chemicals GmbH, Darmstadt, Germany
Na_2HPO_4	NORAS MRI products GmbH, Höchberg, Germany
KH_2PO_4	Merck Chemicals GmbH, Darmstadt, Germany
HEPES	Sigma-Aldrich Co., St. Louis, USA
D-Glucose	Gibco, Life Technologies GmbH, Karlsruhe, Germany
$MgCl_2$	Sigma-Aldrich Co., St. Louis, USA
EGTA	Sigma-Aldrich Co., St. Louis, USA
NaOH	Sigma-Aldrich Co., St. Louis, USA

DMZ-Universal quartz puller	Zeits Instruments, Augsburg, Germany
DMZ-Universal puller	Zeits Instruments, Augsburg, Germany
Inverted microscope	Axiovert 35, Zeiss, Oberkochen, Germany
Upright microscope	Axioscop, Zeiss, Oberkochen, Germany
Axopatch 200B amplifier	Axon Instruments, Foster City, CA, USA
Multi-micromanipulator (MPC-200)	Sutter Instrument, Novato, CA, USA
P810.30 actuator	Physik Instrumente, Waldbronn, Germany
Precision pressure regulator	Festo, Esslingen, Germany
6-port valve (HVX 86915)	Hamilton, Darmstadt, Germany
POWER1401-3 A/D converter	Cambridge Electronic Design Limited, UK
DC analysis programs (DC-Progs)	University College of London, UK
ISO2 software	MFK Computer, Niederhausen, Germany

3.2 Cell culture

The cells used in this study were human embryonic kidney cell-line, 293T (HEK293T) (ATCC®CRL-3216™). HEK293T cells were cultured at 37°C, 5% CO_2, in Dulbecco's modified Eagle medium supplemented with 10% fetal calf serum, 100 units/ml penicillin and 100 µg/ml streptomycin. They were plated on poly-L-lysine coated

coverslips. nAChRs were expressed using transient transfection based on calcium phosphate precipitation (Ausubel et al., 1992). For adult type mouse or human nAChRs, their *α*-, *β*-, *ε*- and *δ*-subunits cDNAs were cotransfected with EGFP cDNAs transiently in the ratio 2:1:1:1:0.5 (Auerbach and Akk, 1998). The chimeric receptors were composed of mouse *α*-subunits and human *β*-, *δ*- and *ε*-subunits expressed in HEK cells with the same subunit stoichiometry ($M_{\alpha}H_{\beta\delta\varepsilon}$). All subunits of human nAChRs and the *ε*-subunits of mouse receptors were coded using pcDNA3 plasmids, while the other mouse subunits *α*, *β* and *δ* were coded using pRc/CMV plasmids. Both vectors are commonly used in the mammalian expression system.

The basic protocol for a Ø 35 mm dish with 250 ml media is as follows: the desired amount of cDNAs (a total of ~ 3 µg) was mixed with 36 µl of 2.5 M $CaCl_2$ solution. One volume of this solution was added quickly to an equal volume of 2×HBSS (NaCl 280 mM, Na_2HPO_4 2.8 mM, HEPES 50 mM, pH 7.2) at room temperature. Once the two solutions were mixed, they were immediately added to the pre-cultured cells within the medium. The cells were then incubated overnight. On the next day, the culture medium was removed from the dish containing the transfected cells and fresh medium with 10% fetal calf serum was added. Afterwards, the transfected cells were further incubated and used in electrophysiological recordings 20 - 28 h later.

3.3 Electrophysiology

Cell-attached configuration During single-channel recording experiments, cells were visualized using an inverted microscope. The measurements were carried out in the cell-attached configuration (Hamill et al., 1981). The physiological solution used in both the measuring chamber and patch pipettes included (mM): NaCl, 162; KCl, 5.3; $CaCl_2$, 2; Na_2HPO_4, 0.67; HEPES, 15; (pH adjusted to 7.4 with NaOH). Additional agonist (ACh) was added to the pipette solution resulting in a concentration of 10 nM or 100 nM ACh. All measurements were done at 20 - 22°C. The cell-attached patches were clamped at -200 mV.

Single-channel recordings Low-noise recordings for distinguishing the current signals from the background noise (Parzefall et al., 1998) were performed with the patch pipettes produced with quartz glass (outer Ø 2.00 mm, inner Ø 1 mm)

and had resistances between 10 - 20 MΩ (Dudel et al., 2000; Stock et al., 2014). The benefits of using the quartz glass are: (1) due to its hydrophobic surface it prevents creeping of fluid. (2) it has better electrical properties than other glass, such as borosilicate glass used for outside-out patches (see below). The quartz pipette was filled with pipette solution only at the very tip part (< 1 mm) in order to reduce capacitive noise. A very low noise level was achieved: 1.5 ± 0.1 (SD) pA root mean square (RMS) at 60 kHz (-3 dB) low pass filtering and 153 ± 30 (SD) fA RMS at 5 kHz (-3 dB) low pass filtering.

Outside-out patch configuration The transfected cells were visualized with an upright microscope setup at 100-fold and 400-fold magnification sequentially. All recordings were made from patches in the outside-out configuration (Hamill et al., 1981). Low resistance patch pipettes of ~ 5 - 10 MΩ were pulled from borosilicate glass capillaries (outer Ø 2.00 mm, inner Ø 1.16 mm) with a DMZ-Universal Puller. The holding potential was set to -40 mV, the resting potential of HEKT cells. The bath solution contained (mM): NaCl, 162; KCl, 5.3; $CaCl_2$, 2; Na_2HPO_4, 0.62; KH_2PO_4, 0.22; HEPES, 15; Glucose, 5.6 (pH adjusted to 7.4 with NaOH). The pipette filling solution contained (mM): KCl, 150; $MgCl_2$, 2; EGTA, 11; HEPES, 10 (pH adjusted to 7.4 with KOH) (Heckmann et al., 1996). Measurements were performed at room temperature (21 - 24°C).

Excised outside-out patches of HEK293T cells were performed as shown in Figure 8. At the instant of achieving the whole-cell configuration, an anticipated resting potential (-40 mV) was applied to the cell. This negative potential prevented the cell from dying quickly, and made the excision of the membrane from the cell easier. All the measurements were carried out in the voltage-clamp mode.

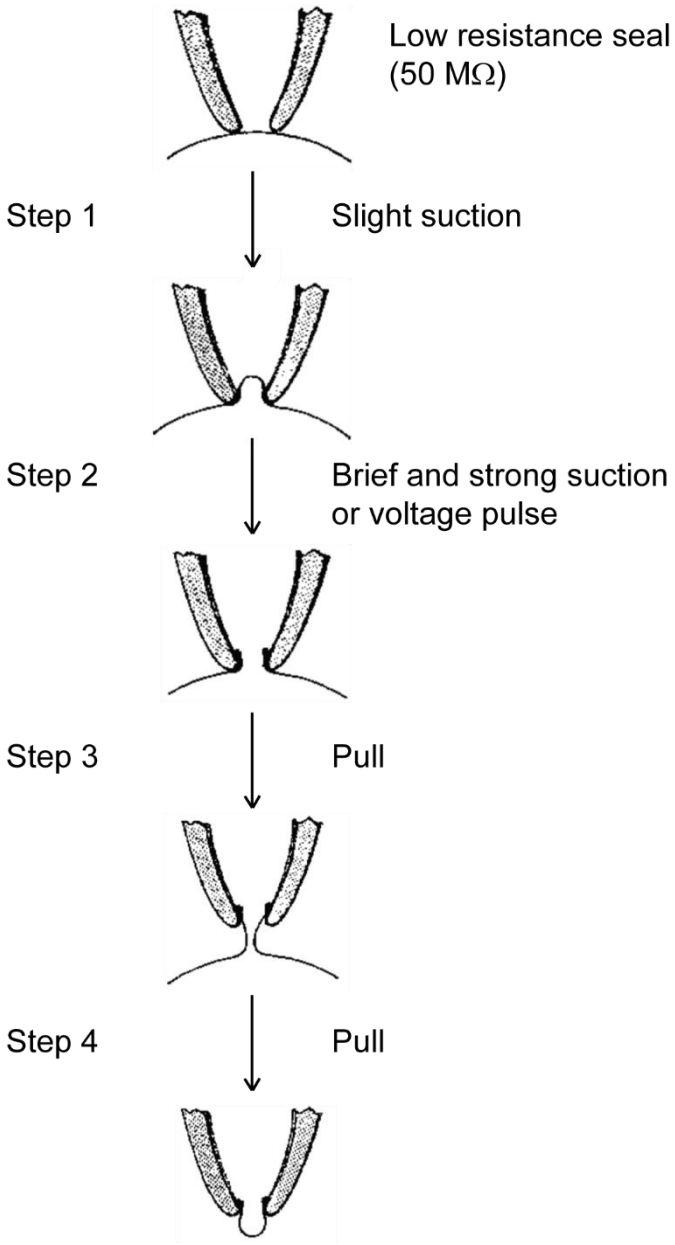

Figure 8. **Schematic diagram illustrating the formation of an outside-out patch.**

Step 1: When a pipette is in contact with the cell membrane with a low resistance seal (around 50 MΩ), a suction is applied and an Ω-shaped membrane vesicle is drawn into the pipette tip forming a gigaohm seal. Step 2: A brief but strong suction is further applied to destroy the cell membrane, allowing the pipette gain access to the cytoplasm. Step 3: The pipette is slowly withdrawn from the cell, allowing a bulb of membrane to bleb out from the cell. When the pipette is pulled sufficiently far away, this bleb detaches from the cell to form an isolated membrane. Step 4: The isolated pieces of membrane reconnect and form a convex structure with the original outside of the membrane still exposed from the pipette (modified from Hamill et al., 1981).

Fast application system ACh was applied at desired concentrations to the excised, outside-out patch with a system for fast drug application (Heckmann and Pawlu, 2002). The apparatus comprises mainly of three parts: a piezo element (P810.30 Actuator), a monoluminal application pipet and an application chamber. The whole application system was mounted on the stage of the upright microscope. The patch electrode was repositioned between the bath chamber and the application chamber by moving the stage horizontally. The movement of the electrode itself was controlled by a micromanipulator. The electrode tip was maintained to be in the solution during the course of an experiment. The relevant parts of the system are shown in Figure 9A.

The piezo held in a brass cylinder was connected with the glass application pipet (outer Ø 0.50 mm and inner Ø 0.30 mm; Hilgenberg, Malsfeld, Germany) which extends 45 µm on application of 100 V, and fixed to the stage using strong magnets. The application pipet was bent to an angle (95 - 110°) (Figure 9B) and placed at the symmetry center of the application chamber (outer Ø 3.00 mm and inner Ø 1.50 mm) via an upper opening. The extracellular solution containing ACh was discharged out of the application pipet forming a thin liquid filament. Syringes (10 ml) served as solution reservoirs. The fluid in the application chamber was the extracellular solution (w/o ACh). The in- and out-flows passing the application chamber were regulated using a pump, while the ACh filament was ejected by hydrostatic pressure. By adjusting the pump and the hydrostatic pressure to vary the speeds of the solutions, a laminar flow pattern was obtained. Care was also taken in the speed of the agonist filament. This was adjusted empirically during application onto a patch. The liquid filament was visualized with DIC (differential interference contrast) optics.

After the outside-out patch was obtained, the excised patch was transferred to the application chamber. Initially the tip of the patch electrode was positioned several µm away from the ACh-containing filament with 0 V applied to the piezo. When a voltage pulse (100 V) was applied to the piezo, the filament shifted toward the patch tip. At the end of the voltage pulse, the filament returned back to its initial position. (Figure 9C). The voltage pulse was produced using ISO2 software. The time course of current changes during the displacement of the filament could be monitored in real time as the channels were activated due to the application of ACh.

A 6-port valve with each port containing a different concentration of an agonist-containing solution was manually operated to flow the solution through the application pipet. For each excised patch, the agonist solutions were applied starting with highest ACh concentration, downgraded step by step, to reduce the “run-down” effect of the system.

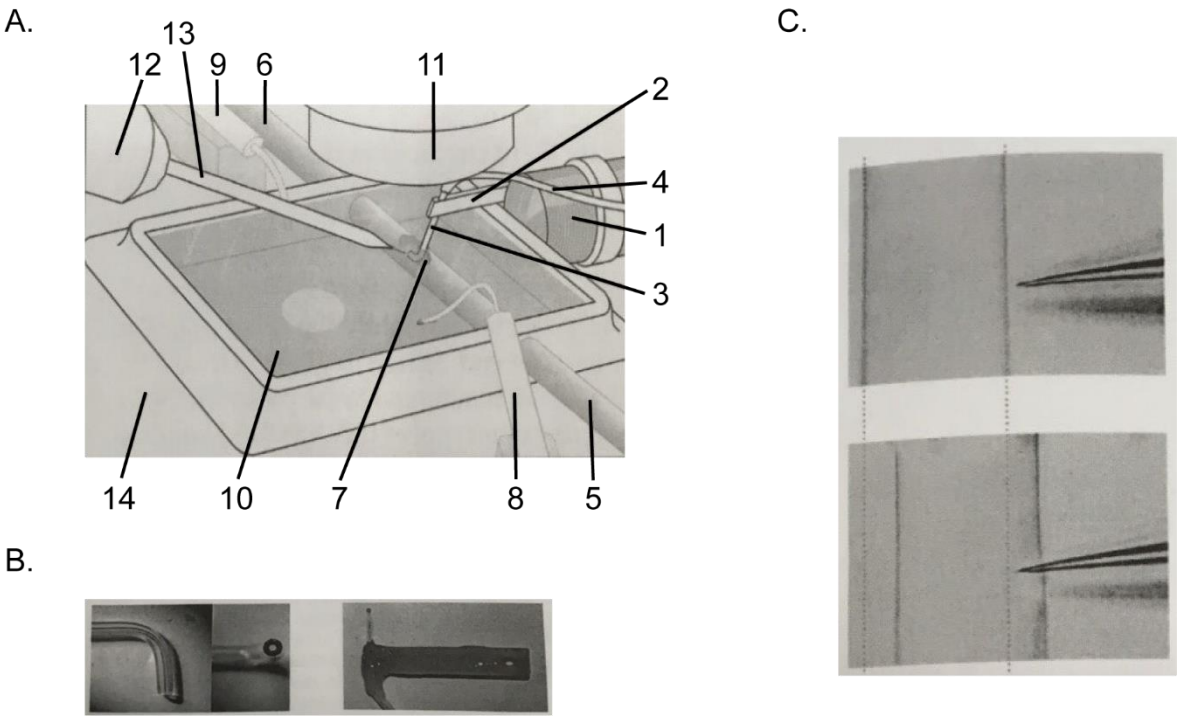

Figure 9. **Illustration of the fast application system.**

(A) Schematic drawing of the fast application system. The piezo element (1), which is fixed to the stage using strong magnets; a platelet (2) to hold the application pipet (3) joint to a tube (4); in- (5) and out-flow (6) of the application chamber (7); in- (8) and out-flow (9) of the bath chamber (10); objective (11); head-stage of the amplifier (12); the electrode (13) for patching and recording; fixed stage (14) of an upright microscope. **(B)** The application pipette was made using a borosilicate glass and glued into a fiberglass platelet. On the left panel, a longer piece of glass was heated using a common lighter to obtain a proper angle for the pipette. On the right panel, the application pipette is glued with a fiberglass platelet to connect with the piezo element (2) in (A). **(C)** The displacement of the liquid filament in response to a voltage pulse, which is applied to the piezo, observed with DIC optics. In the upper image, the initial position of the liquid filament is shown, when 0 V is applied to the piezo. The tip of the patch electrode was placed at the interface between liquid filament and superfusion solution. In the lower image, the liquid filament shifts 45 µm towards the patch electrode with 100 V at the piezo. Dotted lines shows the end position of the filament when 0 V is applied to the piezo (modified from Heckmann and Pawlu, 2002).

Pulse protocols For measuring the affinity of human and mouse nAChRs, ACh with different concentrations (1000 µM, 100 µM, 30 µM, 10 µM and 3 µM) was applied using a single-pulse protocol with a 300 ms duration (100 V applied to the piezo) and a 3 s interval (0 V applied to the piezo) between each pulse. In the antagonist binding affinity experiments, 300 nM α-Bgtx was added to the external solution constantly. The patches were exposed to 30 µM ACh for 30 ms with an interval of 2 s. The potential was hold at -40 mV. To wash out the agonist and antagonist (i.e. ACh and α-Bgtx) with water, the pulse protocol applied to the piezo was set at 0 V, while the liquid filament was kept away from the patch tip.

Half inhibition time To describe the characteristics of the channel blocker, Equation 1 was used to fit the time dependence of peak current amplitudes:

$$I = (\hat{\imath}_a - \hat{\imath}_b)\cdot t_{50}^{n}/(T^{n}+t_{50}^{n}) + \hat{\imath}_b \qquad \text{Equation 1}$$

where $\hat{\imath}_a$ is the initial current amplitude when all channel opened, $\hat{\imath}_b$ is the finial current amplitude after most channels being blocked, and t_{50} is a time period when half channels are blocked, namely “half inhibition time”.

3.4 Single-channel data collection, idealization and time course fitting

Data were recorded, filtered, digitized and stored as described in Parzefall et al. (1998) and Stock et al. (2014). The 4 pole internal 100 kHz low pass filter of Axopatch 200B amplifier was removed, which enabled a recording of the signal with a maximum bandwidth of 130 kHz. The signal was converted at 1 MHz sampling rate with an A/D converter. All data were stored on the hard drive of a PC running Windows XP professional. To reduce noise, the recordings were digitally low-pass filtered at 40 kHz, 3 dB cut off using FILTSAMP (DC software), leading to a filter rise-time of ~ 8.5 µs. After filtering, recordings were down-sampled from 1 MHz to 500 kHz, therefore the sampling frequency was 12.5-fold higher than the -3 dB low-pass filter cut off.

Generally, for reliable detection, the signal to noise ratio is required to be at least 10. The obtained mean signal to noise ratio was 14.2 ± 1.6 (SD). For idealization, the Scan program (DC software) was used. Afterward imposing a resolution of 5 µs,

the open periods were done in EKDIST (DC software). Recordings with unstable baselines or amplitudes were not used for analysis.

3.5 Data acquisition and analysis for macroscopic current responses

Membrane currents were recorded with an Axopatch 200B amplifier with the internal low pass filter at 100 kHz (-3 dB). The output was filtered subsequently with an external 4 kHz low-pass filter. The signals were digitized and stored on the hard disk of a PC 486 using ISO2 software. Digitization was performed at a sampling rate of 12.5 kHz and at 12-bit resolution. Averaging and fitting were performed offline with the ISO2 software.

Statistical analysis and graphics were carried out using Sigmaplot 12.5 software. Since data were not distributed normally, a Mann-Whitney *rank-sum test* was performed for determining the significance when comparing independent groups. Data are given in the form of mean ± s.e.m. (standard error of the mean). The levels of significance are denoted by asterisks: * $P \leq 0.05$, ** $P \leq 0.01$, and *** $P \leq 0.001$.

3.6 Numerical simulations for kinetic modelling

The kinetic model for nAChRs activation (Scheme II in Figure 7) was used. Numerical simulations of the receptor kinetics were performed using a commercial software, ChanneLab. The software solves coupled differential equations through the Runge-Kutta integration method, to generate various sets of rate constants for the receptor behavior during application of ACh. The initial values of the rate constants were taken from Colquhoun and Sakmann (1985). After setting up the parameters for simulations and importing the corresponding stimulus files, numerical simulations were carried out and data generated, i.e. peak current and rise-time, used for plotting the simulated dose-response curves.

To obtain an optimized fit of the simulated dose-response curves, the values of rate constants were changed and the above process was repeated. After optimizing the simulated data compared to the experimental data, the finial estimated values for the rate constants were defined.

3.7 Sequence alignments

The amino acid sequences of nAChR subunits (*α*-, *β*-, *ε*- and *δ*- subunits) and subunits of other receptors were obtained from the Universal Protein Resource (UniProt) database. Alignments were performed by using the online tool ClustalW (Chenna et al., 2003).

4 Results

4.1 Open period distributions in single channel recordings

The initial studies about mouse and human nAChRs were performed at fixed agonist concentration using the ultra low-noise single-channel recording technique (Parzefall et al., 1998; Hallermann et al., 2005). The recordings were done by Dmitrij Ljaschenko and I contributed to the data evaluation. All the measurements were made from patches in the cell-attached mode. To increase the signal to noise ratio, the membrane potential was clamped at -200 mV, which is in addition to the approximate -40 mV of a transfected cell. Recordings were filtered with a low-pass filter at 40 kHz, -3 dB cut-off. A temporal resolution of 5 µs was imposed, which is better than the 6 µs resolution reported by Stock et al. (2014).

Representative open period distributions from recordings at 10 nM and 100 nM ACh are shown in Figure 10. Two sample patches are given at each agonist concentration. In mouse muscle type nAChRs, open period distributions from measurements at 10 nM ACh display two short open period components (Figure 10A). A statistically significant third component was not detected. Open periods are exponentially distributed, and their decay constant τ shows the mean length of channel openings. Here, the open periods were plotted in logarithm *vs.* square root transform. In this case, τ is the peak of the distribution. The peaks of the open periods in one recording are at 37 µs (τ_{O1}) with 65% and 187 µs (τ_{O2}) with 35%, while the components of another patch were at 53 µs (τ_{O1}) with 46% and 209 µs (τ_{O2}) with 53%. The two components represent two open states. Their length is determined by the closing rate constant α. The area (%) indicates how often the event happens. At a higher ACh concentration (100 nM), two further open period components appear, a very short one and a long one. Again, open period distributions of two sample recordings are shown. The long openings are at 787 µs (τ_{O3}) and 1380 µs (τ_{O3}), respectively. The long openings are known to stem from double-liganded receptors, which perform long bursts of openings. Such findings proved to be consistent in all recordings. Therefore, I conclude that at 100 nM ACh, but not at 10 nM, the mouse receptor channels occur double-liganded states and

therefore create long bursts of openings, which sum up to relevant excitatory postsynaptic potentials.

In contrast, the single-channel recordings performed on the human nAChRs clearly show the long openings already at 10 nM ACh. The long component in sample measurements of Figure 10B are at 1400 µs (τ_{O3}) and 1080 µs (τ_{O3}). Since no significant number of long bursts for mouse receptors at 10 nM ACh occurred, this suggests a higher ACh binding affinity in human receptors.

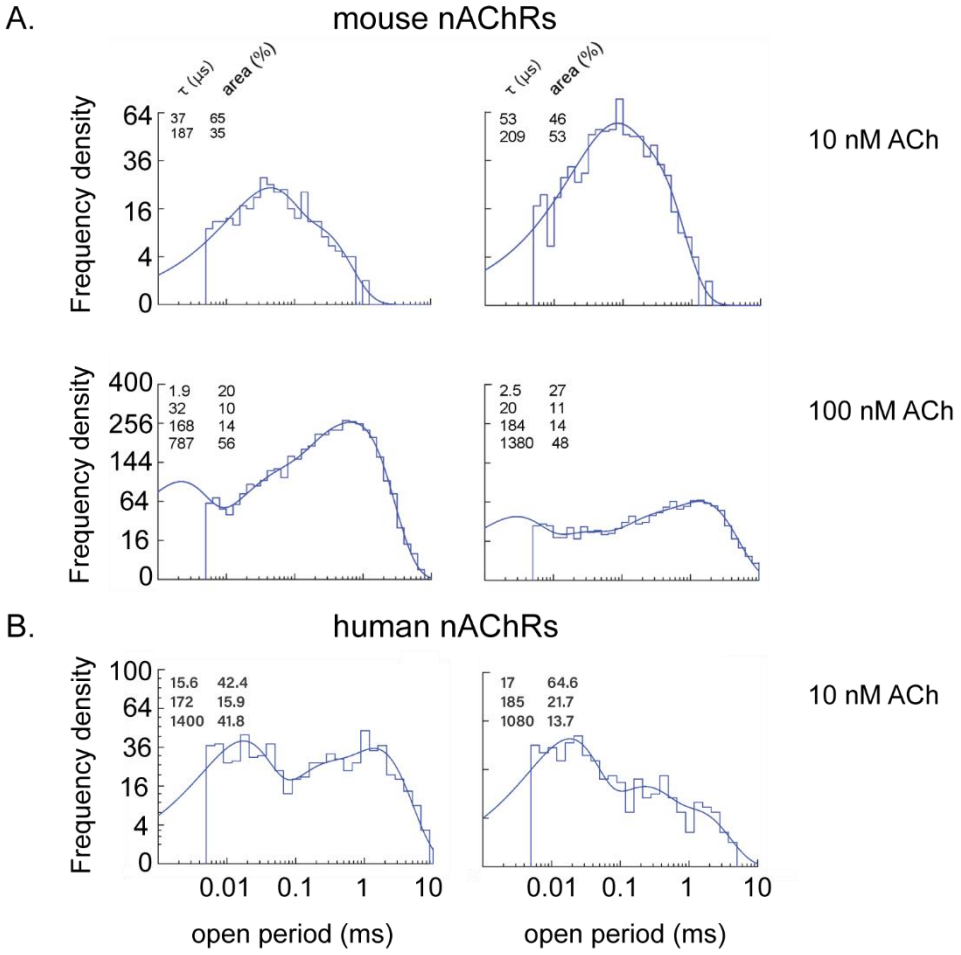

Figure 10. **Open period histograms from single-channel recordings with ACh in mouse and human adult type nAChRs.**

(A) Open period distributions of mouse nAChRs. In the upper row, results of two patches measured at 10 nM ACh display two short open period components in each patch. In the lower row, histograms for two patches recorded at 100 nM ACh. Each patch shows four open period components. **(B)** Open period histograms for human nAChRs from two patches at 10 nM ACh. Each histogram is fitted with three components, including one long opening component. The parameters of the fits are shown within each histogram, τ (µs) and area (%).

4.2 Macroscopic current responses activated by ACh

Based on the findings from single-channel recordings, it appeared to be necessary to test the responses of the receptors at different agonist concentrations in a physiological-like condition. Outside-out patches from cells expressing either mouse or human muscle type nAChRs were held at -40 mV and exposed with a system for fast application to ACh for 300 ms at 3 s intervals. The fast application system can deliver agonists within ~80 µs, a time scale sufficient for studying the quick receptor-openings which are in the order of milliseconds (Heckmann and Pawlu, 2002). Figure 11 shows averaged current traces from one patch with human receptors. Channel openings were elicited with applications of 3 µM to 1 mM ACh. The ACh concentrations applied in such a range can avoid the open-channel block (Sine and Steinbach, 1984, 1987; Ogden and Colquhoun, 1985; Franke et al., 1991a, b). Above 3 µM averaged currents decayed during ACh applications due to desensitization as described earlier (Franke et al., 1991b). Figure 11B shows the initial parts of the normalized traces on an expanded time scale to illustrate the concentration dependence of the current rise-time. Peak current amplitudes were normalized during data evaluation in each recording to the response obtained with 100 µM ACh to obtain $\hat{I}$ (displayed in Figure 12A). The rise-time (t_r) of average currents (Figure 12B) was defined as the time from 10% to 90% of the peak current amplitude (Franke et al., 1991b). Both $\hat{I}$ and t_r are concentration dependent. Recordings of $\hat{I}$ and t_r for all experiments of mouse (grey) and human receptors (black) are summarized in Fig 12 in double-logarithmic plots. At high ACh concentrations $\hat{I}$ reached a plateau due to saturation of the receptors. For the two types of receptors, significant differences of $\hat{I}$ at 30 µM (for mouse: 0.52 ± 0.02 (n=6) and for human: 0.70 ± 0.06 (n=8), $P \leq 0.05$) and at 10 µM ACh (for mouse: 0.19 ± 0.03 (n=9) and for human: 0.33 ± 0.04 (n=10), $P \leq 0.05$) were discovered. Fitting the data with a dose-response curve (not shown) gave half-maximal responses (K_{50}) of mouse receptors of ~ 30 µM ACh compared to ~ 14 µM ACh for human receptors. Furthermore, from 3 to 10 µM ACh, maximum double-logarithmic slopes (Hill slopes) of mouse and human receptors resulted in 1.82 and 1.29, respectively.

The values of t_r in Figure 12B decreased with increasing agonist concentration and t_r reached a lower plateau above 100 µM. With 1 mM ACh, t_r of mouse receptors

was 0.21 ± 0.04 ms (n=5) compared to 0.17 ± 0.02 ms (n=4) in human receptors. Similarly, at low ACh concentrations, t_r also reached a plateau at a maximum value (Franke et al., 1991b; von Beckerath et al., 1995). The values of t_r for mouse and human receptors at 3 µM ACh are 10.20 ± 0.20 ms (n=2) and 4.44 ± 0.76 ms (n=6), respectively. The general concentration dependence is in line with the findings of Franke et al. (1991b), although the t_r values for mouse receptors in this experiment are slightly faster than their value of 0.5 ms at high concentrations, whereas the t_r measured at low concentration are slower than the value of about 5 ms they obtained. Below 1 mM ACh I obtained significant t_r differences for mouse and human receptors. With 100 µM ACh t_r of mouse receptors was 0.44 ± 0.03 ms (n=13) compared to 0.33 ± 0.04 ms (n=12) for human receptors (P ≤ 0.05). Furthermore, with 30 µM ACh t_r of mouse receptors was 1.01 ± 0.11 ms (n=6) and 0.61 ± 0.06 ms (n=8) for human receptors (P ≤ 0.01). Finally, with 10 µM ACh t_r of mouse receptors was 3.05 ± 0.39 ms (n=9) compared to 1.95 ± 0.27 ms (n=10) for human receptors (P ≤ 0.01).

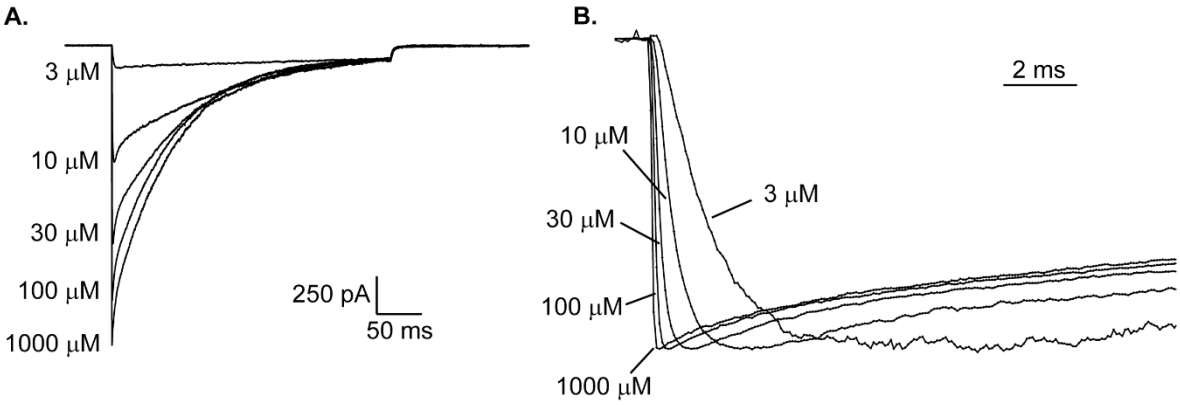

Figure 11. **Averaged macroscopic current responses of human adult type nAChRs on a representative patch at different ACh concentrations.**

(A) Superimposed averages were recorded in the same outside-out patch. The patch was clamped at -40. A 300 ms ACh-pulse was applied with an interval of 3 s. All data were low-pass filtered at 4 kHz and digitized at 12.5 kHz. **(B)** Enlarged onset sections of normalized current responses in (A). Traces were elicited by the indicated concentration of ACh. The rise-time (10 - 90%) for this patch at 1000 µM, 100 µM, 30 µM, 10 µM and 3 µM ACh was 0.16 ms, 0.20 ms, 0.40 ms, 1.05 ms and 2.98 ms, respectively.

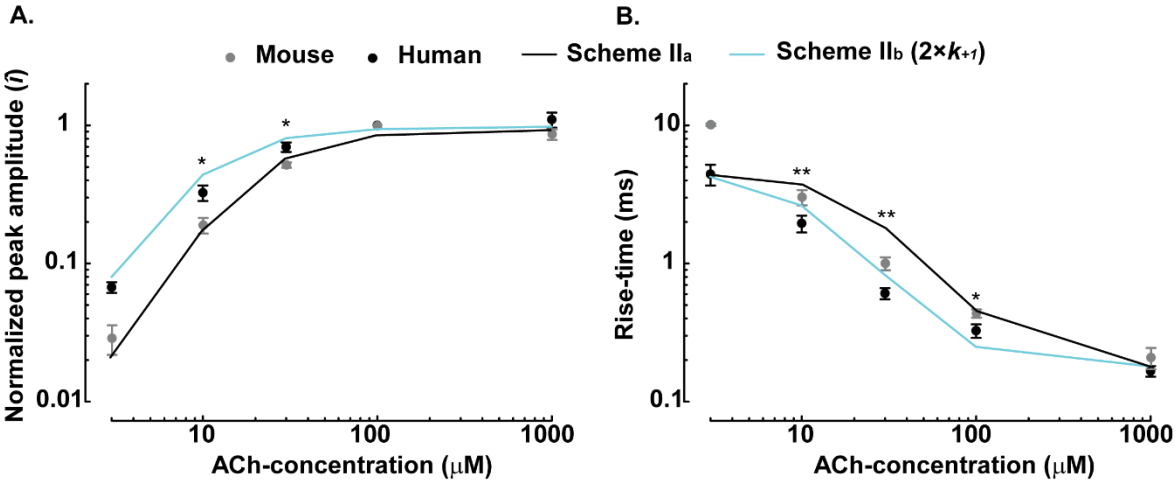

Figure 12. **Concentration dependence of the peak current amplitudes (*i*) and the rise-time (t_r) of mouse and human nAChRs.**

Experimental data shown as points (mean ± s.e.m.) were overlaid by the by the kinetic model Scheme II (Figure 7). The black and blue lines in each graph represent the optimal fit for each type nAChRs using rates in Scheme II_a and II_b (Figure 13). Scheme II_a fits the data of mouse nAChRs with the rate constants: $k_{+1} = k_{+2} = 1.5 \times 10^8$ $M^{-1}{\cdot}s^{-1}$, $k_{-1} = k_{-2} = 20000$ s^{-1}, $\alpha = 1100$ s^{-1} and $\beta = 50000$ s^{-1}. 2, 9, 6, 13 and 5 patches were recorded at 3, 10, 30, 100 and 1000 μM ACh, respectively. For human receptors in each panel, the curves are fitted by Scheme II_b with the following parameters: $k_{+1} = k_{+2} = 3 \times 10^8$ $M^{-1}{\cdot}s^{-1}$, $k_{-1} = k_{-2} =$ 20000 s^{-1}, $\alpha = 1100$ s^{-1} and $\beta = 50000$ s^{-1}. The number of patches averaged at 3, 10, 30, 100 and 1000 μM ACh were 6, 10, 8, 12 and 4 correspondingly. The statistical analysis was performed for comparing the data of mouse and human nAChRs measured at the same ACh concentration (* P ≤ 0.05 and ** P ≤ 0.01, *rank-sum test*).

4.3 Numerical simulation and current fitting

To distinguish the binding and gating steps from the channel activation path, and to interpret the data quantitatively, I recruited the kinetic models for depicting experimental data. According to the maximum double-logarithmic slopes derived from my electrophysiological recordings, both mouse and human receptors are supposed to be activated through two ligand-binding steps. Moreover, referring to the observations in Franke et al. (1991b), I used the same simple reaction model (Scheme II in Figure 7) with two identical binding-sites (Akk and Auerbach, 1996) for numerical simulation of this study. There is no cooperative binding between the two sites. As mentioned before, Scheme II (Figure 7) does not include other reaction processes, such as desensitization and channel openings of mono-liganded receptors.

To find optimal sets of these transition rate constants to fit the experimental data, I systematically tried many intermediate values for each rate constant (k_{+1}, k_{-1}, α and β). Franke and his colleague (1991b) have already elaborated in their paper about the change tendency of the dose-response curves by varying each rate constant during numerical simulations with this simplified model: (1) Binding rate constants have a stronger effect on the dose-response of peak currents than gating rate constants. (2) Increase of k_+ causes the dose-response curves of both $\hat{I}$ and t_r to shift to the left, which is treated as higher affinity of the receptors, but there is almost no change in the rising phases. (3) In contrast, the changes in k_- affect the plateau of t_r greatly, especially at low agonist concentrations, but have little effect on $\hat{I}$ values. (4) The combination of these variations is more complex to estimate and understand superficially. For comparing the receptors affinity, I put more emphasis on varying the values of k_+ and k_-.

The measurements here show that the values of $\hat{I}$ and t_r in mouse receptors are significant different from the corresponding values in human nAChRs at both 30 µM and 10 µM ACh. Thus, the data at these two concentrations are treated as important nodes for fitting the responses. The initial values of these rate constants were taken from the values determined for adult mouse muscle with a similar range of ACh concentrations as in the study by Franke et al.(1991b) ($k_{+1} = k_{+2} = 10^8$ $M^{-1}\cdot s^{-1}$, $k_{-1} = k_{-2} = 20000$ s^{-1}, $\alpha = 1100$ s^{-1} and $\beta = 50000$ s^{-1}). Consequently, the optimal fits for mouse receptors are obtained by increasing the association rate constants based on the initial values, which are of the same order of magnitude: $k_{+1} = k_{+2} = 1.5 \times 10^8$ $M^{-1}\cdot s^{-1}$, $k_{-1} = k_{-2} = 20000$ s^{-1}, $\alpha = 1100$ s^{-1} and $\beta = 50000$ s^{-1} (Figure 12 and Scheme II_a in Figure 13). Likewise, the suitable simulated dose-response curves of both $\hat{I}$ and t_r for human receptors were generated by increasing the association rate constants even higher than that for mouse receptors up to 3×10^8 $M^{-1}\cdot s^{-1}$ and keeping the values of α and β: $k_{+1} = k_{+2} = 3 \times 10^8 M^{-1}\cdot s^{-1}$, $k_{-1} = k_{-2} = 20000$ s^{-1}, $\alpha = 1100$ s^{-1} and $\beta = 50000$ s^{-1} (Figure 12 and Scheme II_b in Figure 13). I had also checked the effect of adjusting the dissociation rate constants by altering k_{-1}. The reduction of k_{-1} from 20000 s^{-1} to 10000 s^{-1} leads similar changes in the simulated dose-response curve of $\hat{I}$ as increasing k_{+1} value. The simulated curve fits the $\hat{I}$ experimental data well (Figure 14A). However, for t_r simulation, the plateau of the

rise-time at low agonist concentrations shifts greatly compared to the experimental data. At 3 µM ACh, the experimental observed value was ~ 4 ms, while the computationally estimated value was ~ 7 ms (Figure 14B). This difference reflects a predicted slower on-rate phase, which does not match the experimental data.

Figure 14 shows the simulated dose-response curves of $\hat{I}$ (Figure 12A) and t_r (Figure 12B) plotted with the optimized set of the rate constants (Scheme II_a for mouse receptors and Scheme II_c for human receptors). It shows that all simulated curves come to a plateau at high ACh concentrations, matching quite well with experimental data. And the curves of $\hat{I}$ seem to fit generally better than the curves of t_r. This is in line with the trends of experimental variations.

Therefore, it can be predicted from the kinetic model that the difference of the affinity between mouse and human receptors is affected predominantly by the binding steps, in particular by the association rate constants. The simulations demonstrate that the association rate constant of human nAChRs are 2-fold of those of mouse receptors, indicating a higher affinity of human compared to mouse receptors for the agonist ACh.

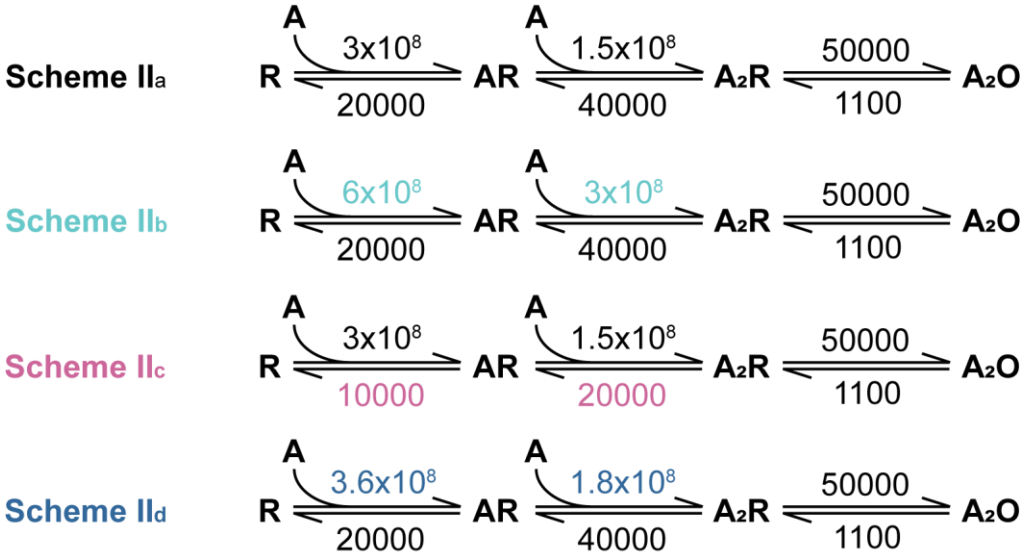

Figure 13. **Parameters estimated for the kinetic Scheme II with two identical binding sites (confer Figure 7).**

Scheme II_a, II_b and II_c were used for the simulated dose-response curves in Figure 12 and Figure 14 with the indicated rate constants. Scheme II_d is used for the dose-response curves in Figure 19.

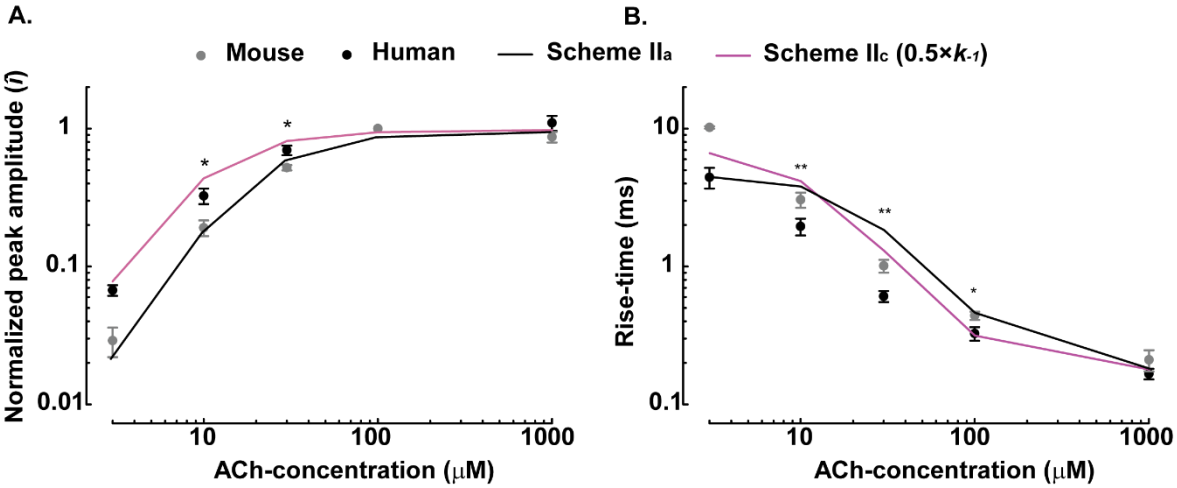

Figure 14. **Simulated dose-response curves of $\hat{i}$ and t_r of mouse and human nAChRs by reducing k_{-} values.**

The simulations were performed by using Scheme II in Figure 7. The black and red lines represent the fits with Scheme II_a and Scheme II_c (Figure 13), respectively. Scheme II_c has the rate constants: $k_{+1} = k_{+2} = 1.5 \times 10^8$ $M^{-1}{\cdot}s^{-1}$, $k_{-1} = k_{-2} = 10000$ s^{-1}, $\alpha = 1100$ s^{-1} and $\beta = 50000$ s^{-1}. Experimental data values (mean ± s.e.m.) and their statistical analysis at the same ACh concentration were the same as in Figure 12. The number of patches averaged at 3, 10, 30, 100 and 1000 µM ACh were 6, 10, 8, 12 and 4 correspondingly (* P ≤ 0.05 and ** P ≤ 0.01, *rank-sum test*).

4.4 Inhibiting effect of α-Bgtx

To further inspect the difference of ligand-binding affinity between mouse and human receptors, the outside-out patches were performed in the fast application system by adding the competitive antagonist α-Bgtx to the background solution. An ACh-pulse was applied for 30 ms with an interval of 2 s. The holding potential was -40 mV, the same as for the step application of ACh.

Comparison of α-Bgtx-affinity of mouse with human receptors was carried out by recording the current responses elicited when competitive binding of ACh and α-Bgtx took place. All of the responses were elicited by repetitive pulses of 30 µM ACh during a wash-in of 300 nM α-Bgtx. Recordings from six patches of both mouse and human receptors are plotted in Figure 15 with the mean values (± s.e.m.) of $\hat{i}$ versus time. The duration of measurement for each patch was not uniform. It varied from patch to patch, depending on the quality of the outside-out patch, as well as on the properties of the two types of receptors. To enable comparison, the traces recorded

during the first 250 s were analyzed for all the current peak amplitudes. Both mouse and human receptors were initially fully activated by ACh, but then gradually got blocked by α-Bgtx. Consequently, it was found that α-Bgtx blocks currents more rapidly in human nAChRs than in mouse receptors. This was the first time that α-Bgtx block was shown using fast agonist application at a high temporal resolution. The antagonist induced a reduction of *î* of human receptors to 26.77 ± 11% at 250 s. In contrast, α-Bgtx attenuated currents to only 63.82 ± 9% in mouse nAChRs (P ≤ 0.05). A first significant difference of the reduction in current amplitudes between mouse and human receptors was detected starting at 130 s (for mouse: 84.53 ± 3% and for human: 46.93 ± 12%, P ≤ 0.05).

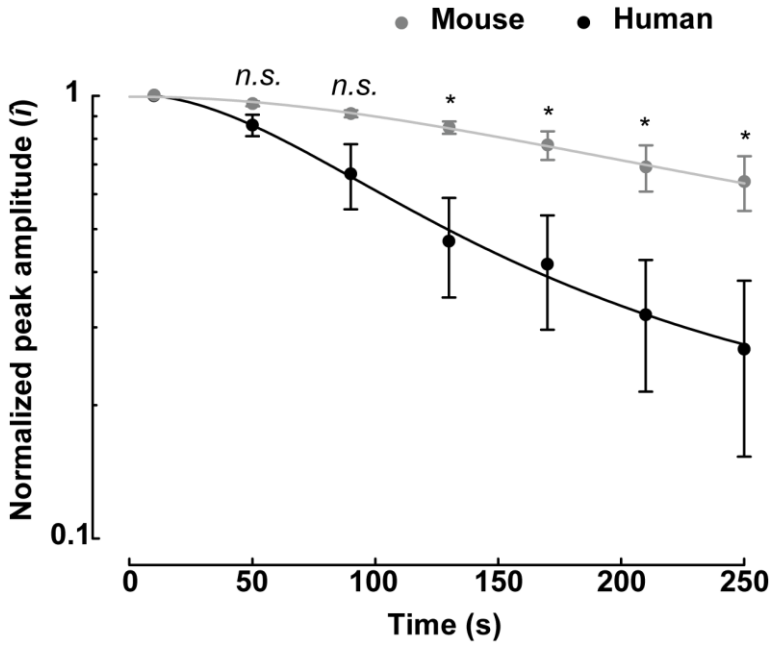

Figure 15. **Time course of α-Bgtx induced nAChR block.**

Current responses of mouse and human nAChRs were recorded during the application of 300 nM α-Bgtx. The membrane potential was kept at -40 mV. A pulse of 30 µM ACh in the presence of background α-Bgtx was applied for 30 ms with an interval of 2 s (n=6 for both mouse and human receptors). Data is presented as mean ± s.e.m. The statistical analysis compared the data of mouse and human nAChRs collected at the same time points (* P ≤ 0.05, *rank-sum test*).

By fitting the curves using Equation 1 (see Materials and Methods 3.3), I obtained the $T_{1/2}$ values, which shows that the time period for half of the mouse receptors to be blocked is ~ 2-fold of the half inhibition time of human nAChRs (for mouse: $T_{1/2}$

= 384.83 ± 41.56 s and for human: $T_{1/2}$ = 160.33 ± 40.60 s, P ≤ 0.05). The competitive antagonist, α-Bgtx can fully occupy both ACh-binding sites and block the receptors. It has been found that competitive antagonists contribute little to the channel-gating behavior (Sine, 2012). Therefore, the current amplitude reductions are most likely due to the alteration occurring at the ligand-binding steps. Thus, this inhibition experiment shows that the α-Bgtx-affinity for human receptors is significantly higher compared to mouse receptors.

4.5 Sequence alignments of various subunits

The results so far raise the questions how such functional difference works, or more specifically, how this difference is related to the genetic difference between mouse and human. To examine the genetic relevance, amino acid sequences were aligned.

Since two *α*-subunits of muscle type nAChRs form the important part of the ligand-binding sites, more detailed analysis of the *α*-subunits was performed. In this study, a comparison of the sequence difference between mouse and human along with the *α*-subunit from the electric fish (i.e. *Torpedo*) was carried out. *Torpedo* receptors have been involved in many classical researches on nAChRs (Wilson et al., 1988; O'Leary and White, 1992; Hucho et al., 1996; Brejc et al., 2001; Karlin, 2002; Cadugan and Auerbach, 2007; Dellisanti et al., 2007a; Prinston et al., 2017). Here, the comparison could provide insights into the relationship between the amino acids evolution and their functional variation among species, which might correlate to their living environment. The sequence alignment displays that all of these different residues can be further distinguished into three groups: (1) residues shared only between human and *Torpedo*, (2) residues shared only between mouse and *Torpedo*, and (3) completely different residues at the same positions among the three species (Figure 16). It is of interest that the proportions of the three groups were similar throughout the amino acids evolution.

To further analyze whether these different residues are related to functional differences between mouse and human receptors, the positions with different amino acids between mouse and human *α*-subunits are marked at corresponding positions in a solved *Torpedo α*-subunit 3D structure (Figure 17). The residues which are known to play an important role in ligand-binding (Arias, 2000) are highlighted. It

was found that most of these amino acids are located in the secondary structures of the ligand binding domain and in the cytoplasmic domain.

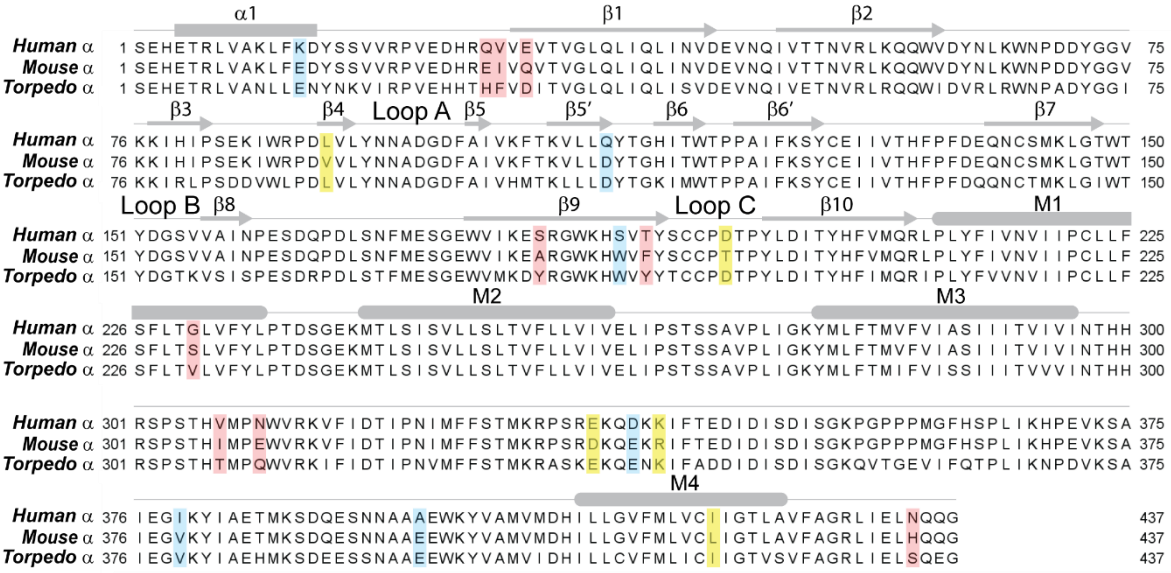

Figure 16. **Amino acid sequence alignment of human, mouse and *Torpedo* nAChR *α*-subunits.**

Residues shared only between human and *Torpedo* are marked in yellow, whereas those only shared between mouse and *Torpedo* are highlighted in blue. Residues, different in all three species, are labeled in red. α1 is a helix structure. β1 - β10 show the structures of β-strands in the ECD. M1 - M4 are the four TMDs. The indicated loop A, B and C join β5 - β5', β7 - β8 and β9 - β10, separately. All key residues located in the loops which are important for ligand-binding are highly conserved among three species.

Figure 17 shows that residues at position 187, 189 and 195 are embedded within a region containing the key amino acids related to the affinity of nAChRs. Therefore, the different amino acids at these three positions are expected to contribute to the affinity difference between human and mouse receptors. This assumption is in line with the different properties of the residues at these positions (more details seen in Discussion 5.4).

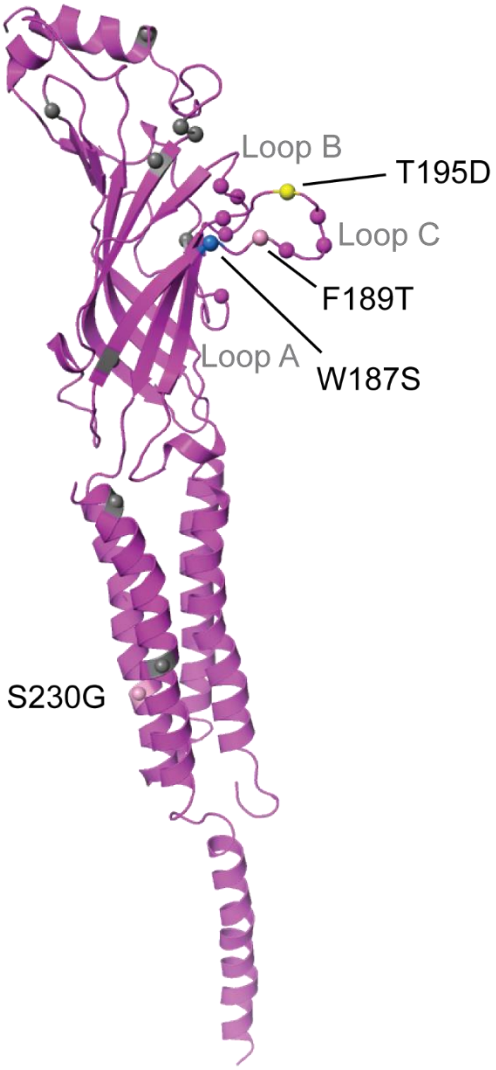

Figure 17. **Amino acid differences between mouse and human *α*-subunits.**

The ribbon diagram illustrates a single *Torpedo α*-subunit (retrieved from the PDB database: 4AQ9). This is merely a part of the real structure except for the cytoplasmic region. Key residues known to be critical to ligand-binding at the N-terminus are marked as spheres in magenta (residues: 93 in loop A; 149, 152 and 153 in loop B; 190, 192, 193 and 198 in loop C). The same structure is shown in Figure 3B. The amino acids, which differ between mouse and human subunits, are indicated as grey spheres. Four of these different residues between mouse and human (colored as blue, pink, yellow spheres according to Figure 16) are potential candidates, which might cause the observed affinity difference. Mouse amino acid is written first, then the position number in the mouse subunit, then the amino acid in the human subunit.

Another potentially important residue for ligand-binding can be at position 230, which is located in the M1 transmembrane domain. Although the contribution of this domain to the nAChRs function is still unknown, several studies which addressed

structure and function have been carried out (Mishina et al., 1985; Suchnay et al., 1993; Akabas and Karlin, 1995; Engel et al., 1996; Wang et al. 1997). Kinetic investigations, based on single channel recordings of mutant mouse adult nAChRs, showed that the M1 domain plays an important role in the channel binding affinity, for example by affecting the dissociation rate (Wang et al., 1997). In human *α*-subunits, at position 230 a Gly^{230} is present, instead of the mouse *α*-subunit Ser^{230}. This difference probably leads to great structural changes (more details also seen in Discussion 5.4).

Additionally, sequence alignment studies on all of the four mouse and human nAChRs subunits (*α*, *β*, *γ* and *ε*), as well as a comparison to other receptor subunits between mouse and human are summarized in Figure 18. Surprisingly, it was found that mouse and human *α*1-subunits share higher identity (95%) and similarity (98%) compared to the other muscle type non-*α*-subunits (~ 88% and ~ 93%). On the other hand, although these two homologous receptors are known to be highly conserved, the subunits of nAChRs appear to have a relatively lower conservation than subunits of GABA1, NR1 and GluK2. This lower conservation could be the reason for significant functional differences between mouse and human nAChRs.

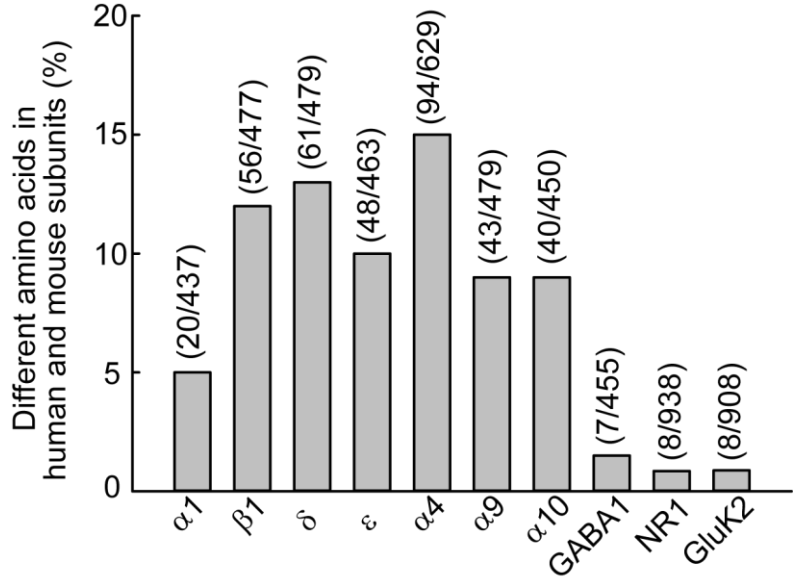

Figure 18. **Amino acid differences among the subunits of mouse and human receptors.**

Bar plot shows the percentage difference of the amino acids in various subunits between mouse and human. The values in the brackets indicate the number of different residues and the length of each subunit.

Comparison of other *α*-subunits (*α*4, *α*9 and *α*10) between mouse and human reveals even greater differences (Figure 18). However, 50% of amino acid differences in the *α*1-subunit are located within the ECD, whereas in *α*4-, *α*9- and *α*10-subunits only 6%, 19% and 28% of the different amino acids are situated there and a very high portion of the different residues is located at the ICD. Therefore, the observed differences in the affinity between mouse and human muscle type receptors could be due to the functional-related sequence differences, especially in the ECD, of their *α*-subunits.

4.6 Experimental responses of chimeric receptors

To address the question whether *α*-subunits are responsible for the observed differences in affinity between mouse and human receptors, chimeric receptors composed of mouse *α*-subunits and human *β*-, *δ*- and *ε*-subunits expressed in HEK cells were generated ($M_{\alpha}H_{\beta\delta\varepsilon}$). The ACh-induced current responses were measured by using the same agonist concentrations and pulse protocol as those performed in experiments for Figure 12.

Analysis of the recordings shows that there is a significant difference in current amplitudes between human and chimeric $M_{\alpha}H_{\beta\delta\varepsilon}$ receptors at low ACh concentration of 3 µM (for human: 0.067 ± 0.001 (n=6) and for $M_{\alpha}H_{\beta\delta\varepsilon}$: 0.035 ± 0.013 (n=7), $P \leq 0.05$). Macroscopic amplitudes are a measure of the number of functional receptors per patch. Interestingly, no significant difference was observed between the rise-times (Figure 19). The finding supports my hypothesis that *α*-subunits affect the channel activation behavior. Next, I applied the numerical simulation using the same kinetic model as in previous analysis (Scheme II in Figure 7). Consequently, a set of parameters was obtained: $k_{+1} = k_{+2} = 1.8 \times 10^8\ M^{-1}{\cdot}s^{-1}$, $k_{-1} = k_{-2} = 20000\ s^{-1}$, $\alpha = 1100\ s^{-1}$ and $\beta = 50000$ (Scheme II_d in Figure 13), with which the simulated dose-response curves were plotted (Figure 19). The association rate constants (k_+) of chimeric $M_{\alpha}H_{\beta\delta\varepsilon}$ receptors are smaller than that of human nAChRs, but larger than the k_+ values of mouse receptors. The experimental data combined with the estimated association rate constants indicate that the lower affinity of $M_{\alpha}H_{\beta\delta\varepsilon}$ receptors was caused by a slight reduction in the association rate constants as a result of introducing mouse *α*-subunits into the human receptors.

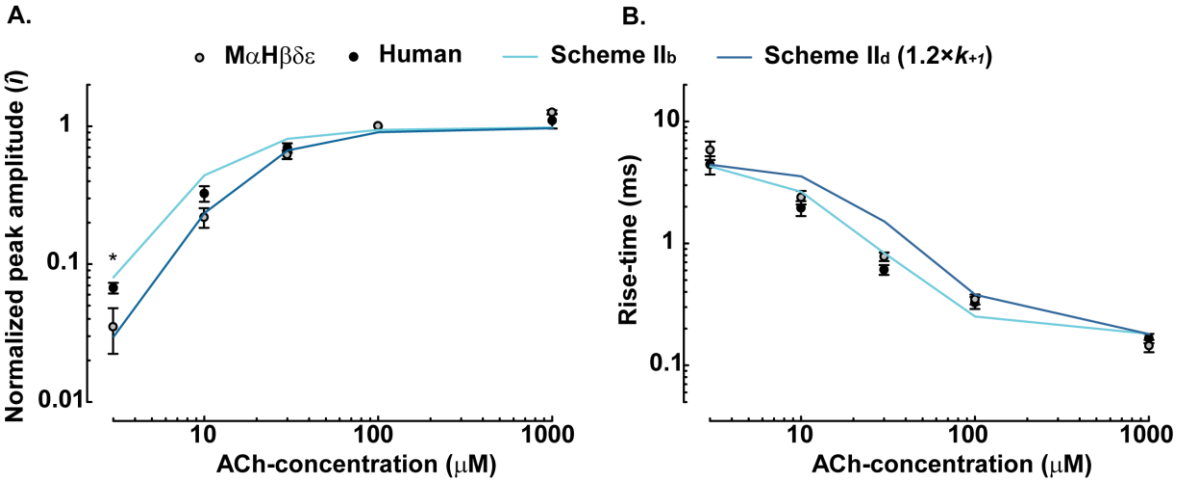

Figure 19. **Concentration dependence of the peak current amplitudes (*i*) and the rise-time (t_r) of human and chimeric $M_\alpha H_{\beta\delta\varepsilon}$ nAChRs.**

Experimental data are shown as points (mean ± s.e.m.). The blue and dark blue lines represent the simulated curves for human and chimeric $M_\alpha H_{\beta\delta\varepsilon}$ receptors using Scheme II_b and Scheme II_d (Figure 13). Data points of chimeric $M_\alpha H_{\beta\delta\varepsilon}$ nAChRs are fitted by Scheme II_d with the following rate constants: $k_{+1} = k_{+2} = 1.8 \times 10^8$ $M^{-1}\cdot s^{-1}$, $k_{-1} = k_{-2} = 20000$ s^{-1}, $\alpha = 1100$ s^{-1} and $\beta = 50000$ s^{-1}. The number of patches averaged at 3, 10, 30, 100 and 1000 μM ACh were 6, 10, 8, 12 and 4, respectively. M, mouse. H, human. The statistical analysis compared the data of chimeric and human nAChRs measured at the same ACh concentration (* $P \leq 0.05$, *rank-sum test*).

5 Discussion

In the present study, an affinity difference between mouse and human adult nAChRs was uncovered and quantified. Human receptors have a higher affinity for both ACh and α-Bgtx than mouse receptors. The quantification of ACh affinity shows a two-fold higher association rate in human nAChRs. The chimeric $M_{\alpha}H_{\beta\delta\varepsilon}$ receptors are functional and have an intermediate ACh association rate. On that account, an important role of the *α*-subunits in influencing the receptor affinity was discovered. Several key residues within the ACh-binding pockets have been identified, which putatively affect the receptor's affinity. This could help in deciphering the nAChR structure-function relationship and in understanding how the different properties of the receptor, such as sequence differences, influence receptor function in various species.

5.1 Subunit composition and affinity

Experiments with the fast application system, i.e. macroscopic recordings, in this study point to a significantly higher affinity for ACh in human compared to mouse nAChRs. This finding confirms the observations in single-channel recordings (Figure 10). Data collected from the macroscopic current responses are more practical for generating dose-response plots, where agonist affinity is studied based on ensemble properties, than from microscopic single-channel currents (Edelstein et al., 1996). The dose-response experiments on the chimeric $M_{\alpha}H_{\beta\delta\varepsilon}$ nAChRs, in which the human *α*-subunits were exchanged by the mouse *α*-subunits, showed a lower affinity than that of human nAChRs. Assisted by the kinetic model (Scheme II in Figure 7), the ligand binding effect was quantitatively analyzed through dose-response simulations. The optimal rate constants were estimated by fitting the dose-responses of $\hat{\imath}$ and t_r (Figure 12 and Figure 19). The channel opening rate (β) was found to be 50000 s^{-1}. This value is close to the value (50000 - 60000 s^{-1}) for human adult nAChRs obtained by Sine et al. (1995) from their single-channel recordings at ACh concentrations ranging from 50 to 300 nM. For mouse adult nAChRs, the ACh association and dissociation rates (k_+ and k_-) estimated from single-channel current responses were ~ 3×10^8 $M^{-1} \cdot s^{-1}$ and 50000 s^{-1}, respectively (Wang et al., 1997; Salamone et al., 1999; Bouzat et al., 2000). The estimated values in the present investigation are in the same order of magnitude as the previous findings (for mouse:

k_+ = 1.5 × 10^8 $M^{-1}{\cdot}s^{-1}$, k_- = 20000 s^{-1}; for human: k_+ = 3 × 10^8 $M^{-1}{\cdot}s^{-1}$, k_- = 20000 s^{-1}). Simulations for the chimeric $M_\alpha H_{\beta\delta\varepsilon}$ receptors showed an association rate (1.8 × 10^8 $M^{-1}{\cdot}s^{-1}$), which lies between the values of mouse and human nAChRs, while other parameters remained unaffected. Therefore, the substitution of *α*-subunits primarily alters the agonist association rate.

The affinity of the receptors for the competitive antagonist (α-Bgtx) was also studied. Previous binding experiments found ^{125}I-labeled Bgtx has a higher binding affinity for human than mouse nAChRs (Ishikawa et al., 1985). However, there is a possibility that the fluorescent agents or the conjugated radioactive isotopes altered the binding properties of the toxin for the receptor. Here, unmodified α-Bgtx was used in the fast application patch clamp experiments. This made it possible to examine the toxin affinity via its inhibitory effect on the receptors in its natural state. The result shows that human nAChRs have a significantly higher affinity for α-Bgtx than mouse receptors. However, whether *α*-subunits cause a lower affinity for α-Bgtx in mouse receptors still needs to be determined. Experiments to test the toxin affinity of the chimeric $M_\alpha H_{\beta\delta\varepsilon}$ receptors would be required. If the current responses of the $M_\alpha H_{\beta\delta\varepsilon}$ receptors display a significant decrease compared to human nAChRs (with a similar method as in Figure 15), it would be possible to conclude that *α*-subunits contribute to the different affinities for α-Bgtx between two species.

5.2 Various kinetic models

The extended del Castillo and Katz mechanism (Scheme II in Figure 7) has been generally used for analyzing both adult and embryonic nAChRs activations (Colquhoun and Sakmann, 1981; Sine and Steinbach,1986a, b; Auerbach and Linglet, 1987). Based on Scheme II, a modified model, which contains an additional mono-liganded open state of the receptor (Scheme III in Figure 20) was proposed by Karlin (1967). However, at high agonist concentrations, mono-liganded open states exist but are not considered to be important for the channel opening (Colquhoun and Sakmann, 1981, 1985; Labarac et al., 1985). This is consistent with the findings of the single-channel recordings in the present study. The long component in the open period distributions of mouse nAChRs at 100 nM ACh represents the largest proportion (~ 50% area) among all the components (Figure

10A). Therefore, measurements at high agonist concentrations, where the majority of the channel opening events are induced by double-liganded, active receptors, make the observations easier to understand. Several laboratories have reported the two binding sites (*αδ*- and *αε*-site) to be almost equivalent in adult nAChRs (Franke et al., 1991b; Akk and Auerbach, 1996; Wang et al., 1997; Salamone et al., 1999). This is different in embryonic receptors, where ACh binds to the *αδ*-site with much higher affinity, compared to its binding to the *αγ*-site (Zhang et al., 1995; Stock et al., 2014). Therefore, as mentioned above, the four-state Scheme II with two equivalent binding-sites is taken to be adequate for depicting adult nAChRs.

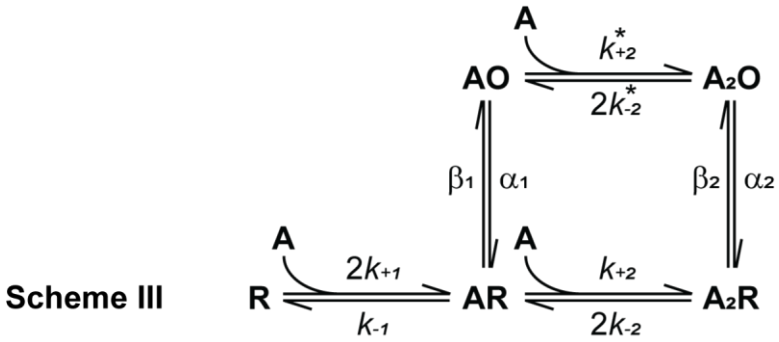

Figure 20. **Reaction scheme with the mono-liganded open state.**

Based on Scheme II, Karlin (1967) proposed Scheme III, which is based on Scheme II but with an additional mono-liganded, open-state of the receptor (AO). This intermediate open-state can be further liganded by another agonist. When double-liganded, the receptor comes to another open state (A_2O). In this scheme, more rate constants than in Scheme II are included (i.e.: k_{+2}*, k_{-2}*, α_1 and β_1). These rate constants are constrained by each other in a semi-cyclical path. The equilibrium between the two open states (AO and A_2O) is defined by k_{+2}* and k_{-2}*. k_{+2}* is agonist concentration dependent. As in Scheme II, the affinity for the agonists at two binding sites are assumed to be identical.

With respect to a finer feature of the receptor binding-gating process, a model with an intermediate “flip-state” was introduced (Lape et al., 2008; Scheme IV in Figure 21A). Scheme IV allows the reaction rates of the channel activation to be investigated in more detail. The flipping model has been used for comparing the effect of the full agonist with that of the partial agonist (Figure 21B). The current response to partial agonists is smaller, which is limited by an inefficient conformational change (the flipping) before channel opening.

A.

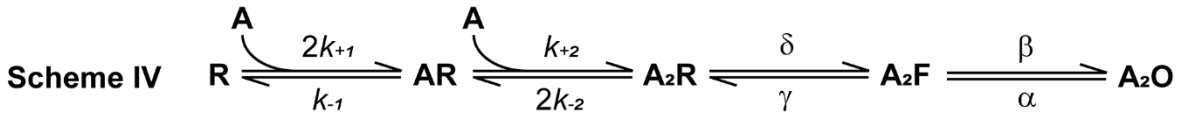

B.

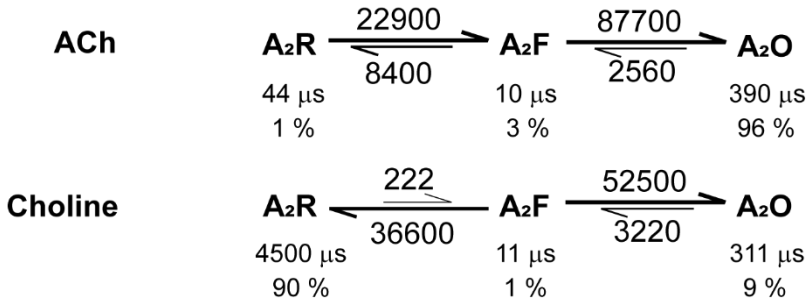

Figure 21. **The "flip" nAChR kinetic model.**

(A) "Flip" model without mono-liganded binding step. Scheme IV includes a pre-opening conformational change ("flip") in the activation path. A_2F represent the double-liganded pre-opening flipped state. The channel can open afterwards. The receptor flipping reaction differs between agonists (modified from Lape et al., 2008). **(B)** Activation of the receptor by ACh and choline. The rate constants for channel flipping (*δ* and *γ*) and opening (*β* and *α*) are shown. The sizes of the arrows are related to the values of the transition rates. The gating reaction is similar for ACh and choline. The low gating efficiency of the partial agonist choline stems from its inability to stabilize the flipped state. The mean lifetime of each state (μs) and the proportion of time (%) spent in each of the states are shown at equilibrium. The A_2R occupied by choline stays much longer (90%) than that by ACh (1%), followed by a quick flip-state (1%). The receptor occupied by ACh stays in the flip-state a bit longer (3%). The mean lifetime of the open states are similar for both ACh (390 μs) and choline (311 μs), whereas the opening probability of the receptor is 96% for ACh, but only 9% for choline. ACh, full agonist. Choline, partial agonist. Values for ACh are from Lape et al., 2008. Choline values are from Lape et al., 2009.

For the present study, it would be interesting to compare the affinities by using partial agonist choline. It is another natural agonist for nAChRs and the precursor of ACh. The choline affinity for the receptor flip-state (A_2F) is lower than for the closed state (A_2R). As a consequence, the receptor occupied by choline spends more time in its closed state (A_2R). Therefore, an even lower number of open mouse nAChRs are expected through choline association.

5.3 Simulation of synaptic responses at the NMJ

The time course of opening events of the postsynaptic nAChRs is determined mostly by the binding- and gating-rates of the receptor. It is possible to simulate a physiological-like process between synapses using well-estimated rate constants.

The simulations carried out in this study focused on the properties of the receptors without concerning such features as the receptor surface geometry or the spatial distribution of the receptors and agonist molecules. The software (ChanneLab) employs a deterministic approach using ordinary differential equations (ODEs) to describe the reaction mechanisms. The advantage of this one-dimensional approach is the ability to integrate the ODEs rapidly and predict the average behavior of the receptors. However, this approach does not take into account the spatial features present in a realistic physiological condition.

Simulation programs are available to model more realistic conditions. MCell, for example, is one such software, which is used extensively. It is based on Monte Carlo algorithms to simulate the diffusion of agonists and their interaction with the receptors, in combination with 3D synaptic reconstructions (https://mcell.org). Figure 22 shows a 3D reconstructed postsynaptic membrane at the NMJ by using the MCell programme. The software is capable of providing snapshots of the synaptic transmission at any point in time. By simulating the diffusion and binding of ACh molecules to nAChRs with stochastic interactions in 3D, the spatial distribution of target nAChRs in various states can be obtained. From these data, the efficiency of the synaptic transmission can be predicted, such as the amplitudes and the time course of the miniature endplate currents (mEPCs). The results obtained from these simulations compare well with average values from experimental measurements (Stiles et al., 1996; Pawlu et al., 2004).

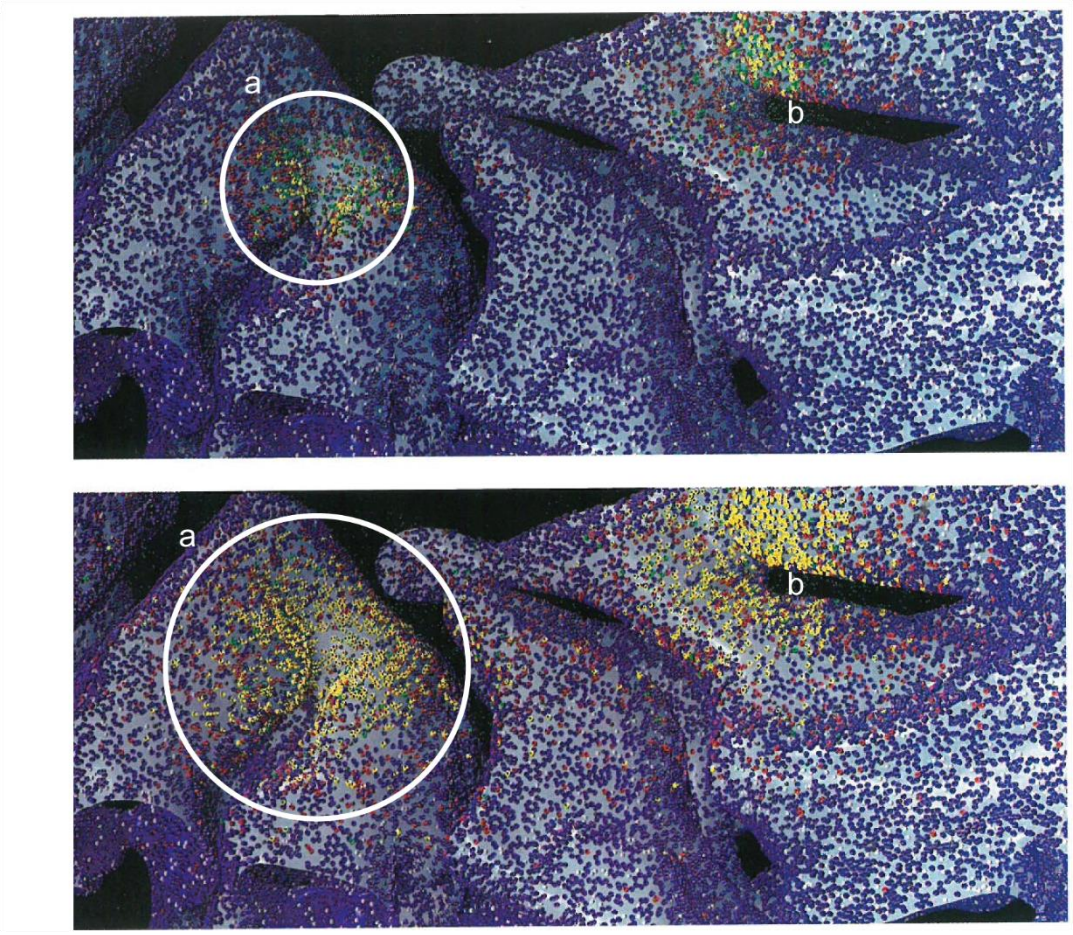

Figure 22. **Time course simulation of ACh binding to nAChRs at the NMJ.**

Snapshots of the synaptic transmission were taken in MCell at 100 µs (upper panel) and 400 µs (lower panel) after the release of ACh from presynaptic vesicles. Two sites (**a** and **b**) are shown, which correspond to two different presynaptic AZs (not shown). The area of site **a**, which contains double-liganded, activated receptors, is marked with a white circle as "saturated disc". For example, at 100 µs, 387 activated receptors within a Ø 0.3 µm saturated disc (upper panel) are present. At 400 µs, 687 receptors are activated (lower panel) in the extended saturated disc of Ø 0.5 µm. This simulation can demonstrate the effect of the affinity on the receptor activity, which causes the postsynaptic mEPCs. The time course of receptor opening is mostly determined by the rates of binding and gating, as well as receptor spatial distribution. Receptors on the postsynaptic membrane are color-coded according to their states (unbound state R, blue; single-liganded state AR, red; double-liganded, inactive state A_2R, green; double-liganded, active state A_2O, yellow). The size of each image is 1.7 × 0.7 µm (modified from Stiles et al., 2003).

Therefore, MCell can be used to simulate the mEPCs generation at the mouse and human NMJs according to the affinity parameters observed. These simulations would help to understand how the affinity affects the efficiency of the synaptic

transmission quantitatively, which has been little known in the synaptic physiology in human.

5.4 Interpretations of the candidate key residues effects

***α*-subunits** Investigators of adult nAChRs have demonstrated that the ligand-receptor interaction takes place at the binding-sites formed at the *α*-*δ* and *α*-*ε* surfaces (Ishikawa et al., 1985). Although the binding sites for ACh and α-Bgtx have an overlap, the key residues involved in their binding are not entirely identical (Arias, 2000; Dellisanti et al., 2007a, b). In this study, the contribution of *α*-subunits to the ligand-binding effect was exemplified through the dose-response experiments of the chimeric $M_{\alpha}H_{\beta\delta\varepsilon}$ receptors. Their k_{+1} value lying between mouse and human nAChRs indicates a reduction in ACh affinity caused by mouse *α*-subunits, when interacting with non-*α*-subunits of human receptors. The amino acids in the *α*-subunits are highly conserved between mouse and human nAChRs. Sequence alignments revealed that, among the few different residues, about 50% of the differences in the muscle type *α*-subunits are located in the ECD. This is a much higher proportion than for the other subunits (see Results 4.5). Thus, it is interesting to further understand how the structural and molecular-interaction characteristics of mouse and human *α*-subunits affect the receptor properties.

The amino acids 93 to 198 form loops A, B and C (Figure 4). Loop C (residues around 176 - 209) was found to contribute predominantly to the ligand-binding (Sine, 2002). There are 10 amino acids that are different in the ECDs of human and mouse nAChRs. Four of these are located in loop C (Figure 16). Among them, three residues (at positions 187, 189 and 195) are considered to contribute to the different affinities between the two species. The fourth residue (at position 181) is close to the three residues in the receptor's primary structure (Figure 17), but it is not thought to be a candidate due to its spatial position far from the loop C.

Residues 187 and 189 are known to participate in both ACh- and α-Bgtx-binding (Sine, 2002; Figure 5B). Several kinetic studies performed in HEK293 cells indicate that mutations of both residues reduce the affinity for α-Bgtx through their impact on the association process (Kreienkamp et al., 1994; Keller et al., 1995). The present study supports this conclusion. It was found that residue 189 is located at the center

of the toxin-receptor interface, most likely interacting with the toxin directly. Residue 187 is located at the peripheral region and mainly stabilizes the interacting structure (Dellisanti et al., 2007b). The residues Trp^{187} and Phe^{189} in mouse *α*-subunits are replaced by Ser^{187} and Thr^{189} in human subunit, respectively. Ser^{187} and Thr^{189} belong to the group of polar-uncharged amino acids, which can form hydrogen bonds with ligands and confer specificity onto receptor-ligand interaction. Therefore, the amino acids at these two positions appear to generate a higher affinity for both ACh and α-Bgtx in human nAChRs. On the other hand, the aromatic residues Trp^{187} and Phe^{189} in mouse *α*-subunits are capable of interacting with other aromatic amino acids and the positively-charged groups. Such properties are important for forming closed scaffolds within proteins, but they have not been proven to play a role in ligand-binding.

Candidate residue 195 is negatively charged in human *α*-subunits (Asp^{195}), while it is uncharged at the corresponding position in mouse subunits (Thr^{195}). Both are polar and hydrophilic. The residue at this position had not been reported to contribute to ligand-binding directly (Arias, 2000; Sine, 2002). However, it is situated in close proximity to the cysteines $Cys^{192,193}$, which play a major role in agonist-binding (Kao and Karlin, 1986). Although this cys residue pair itself is not required for α-Bgtx binding (Griesmann et al., 1990; Spura et al.,1999), amino acids in its proximity, such as residue 194, have been found to contribute to conformation changes when interacting with the toxin (Neumann et al., 1989; Barchan et al., 1992, 1995; Kachalsky et al., 1995; Dellisanti et al., 2007b). Thus, there is a possibility that the residue 195 affects the ligand-binding due to its proximal location.

In addition to the residues mentioned above, residue 230 in the M1 segment, also presents itself as a candidate. In fact, most residues in M1 are known to be highly conserved. Residue Gly^{230} in mouse *α*-subunits is occupied by Ser^{230} in human subunits. Gly, as the smallest amino acid, can fit into narrower spaces, giving it an amphoteric property. Also, Gly does not help in helix formation. Therefore, compared to mouse nAChRs, residue Ser^{230} in human subunits appears to cause a prominent structural change of the M1 segment. Such a structural change could lead to an alteration at the binding-sites and thus result in binding affinity changes.

Non-*α*-subunits Since the two binding-sites are located at the interfaces of two subunits, the contribution of the neighboring non-*α*-subunits can not be neglected. It is known that most *α*-subunits have strong functional constrains (Tsunoyama and Gojobori, 1998). And the less conserved non-*α*-subunits provide functional specificity for various nAChR subtypes (Sine and Engel, 2006). Previous studies have suggested that the genes of the ancestors of *β*-, *δ*-, *γ*- and *ε*-subunits might have been co-regulated by each other to some extent. The k_{+1} value of the chimeric $M_{\alpha}H_{\beta\delta\varepsilon}$ receptors is higher than that of mouse receptors, but not as high as that of human receptors. This result is in agreement with the idea that non-*α*-subunits can also affect the receptor affinity. The sequence alignments of the non-*α*-subunits (Figure 23) reveal that several residues located in the supplementary binding loops (loops D, E, F and G) are different between mouse and human nAChRs. These residues are likely to be critical in shifting the affinities, either by interacting with ligands directly or through their interaction with *α*-subunits.

In *δ*-subunits, four residues of the known key amino acids in binding loops (Arias, 2000) are different between human and mouse (Figure 23A). The amino acids at these four positions are the same between mouse and *Torpedo*, a primitive vertebrate, indicating that the changes seen in human receptors are due to the molecular events that occurred later in evolution. In loop D, the hydrophilic and polar Ser^{37} of mouse receptor is replaced in human by Ala^{37}, a hydrophobic and nonpolar residue. Similarly, in loop F, the polar Tyr^{117} and the hydrophilic Thr^{119} in mouse are substituted by nonpolar Phe^{117} and hydrophobic Tyr^{119} respectively in human. Hence, residues 37, 117 and 119 might affect the affinity of nAChRs. In addition, the residue 60 is also different between mouse and human. These amino acids, however, have similar properties (Glu^{60} in mouse and Asp^{60} in human). Thus, this residue replacement between mouse and human nAChRs may be functionally neutral.

Between human and mouse *ε*-subunits, there are two amino acids (residues 115 and 117) that are different in the binding loops (Figure 23B). In human receptors it was found that, when Pro^{121} is replaced by Leu^{121}, the ACh affinity of the open-state nAChRs is reduced by 500-fold. In contrast, little change was observed in the affinity of the close-state receptors (Ohno et al., 1996). Residue 115 is arranged spatially

close to residue 121. Since the aromatic residue Tyr[115] in mouse subunits is exchanged for Ser[115] in human *ε*-subunits, residue 115 could be considered to influence ACh affinity. On the other hand, residue 117 has similar properties in human and mouse receptors, thus it is unlikely to affect affinity.

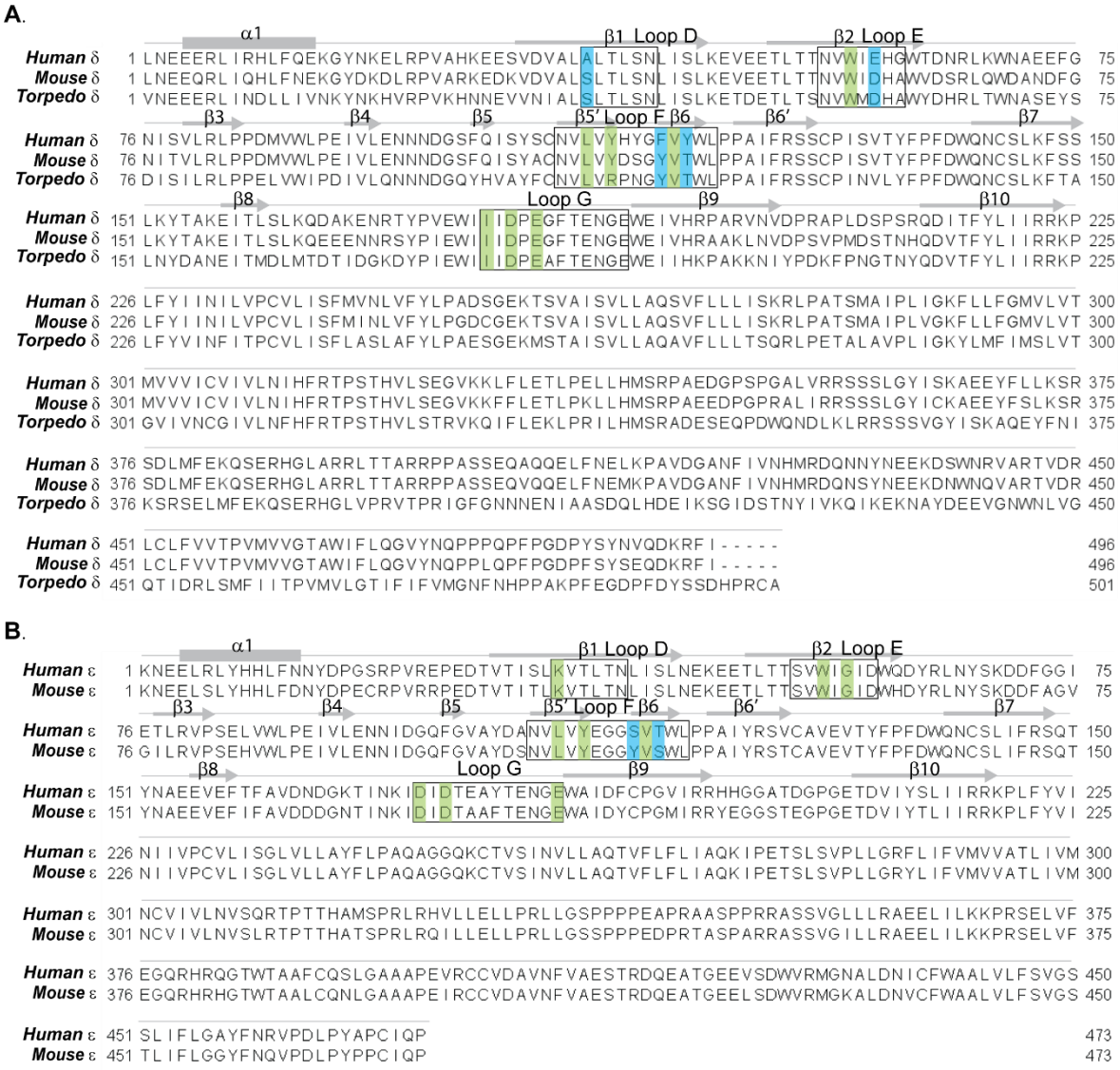

Figure 23. **Sequence alignment of *δ*- and *ε*-subunits from human and mouse nAChRs.**

(A) Alignment of *δ*-subunits. **(B)** Alignment of *ε*-subunits. Loop D, E, F and G at the *α*-*δ* or *α*-*ε* ligand-binding site are marked with frames. The critical residues for ligand-binding in each loop are highlighted in green. In case there are differences between the mouse and human subunits, the amino acids are highlighted in blue. In *δ*-subunits, the residues that differ are S36A, D59E, Y117F and T119Y (highlighted in blue). In *ε*-subunits, only two residues are different between mouse and human subunits, Y115S and S117T (highlighted in blue). They are both in loop F. Note that there are *γ*-subunits in *Torpedo* receptors, therefore the alignment of *ε*-subunits is only between human and mouse receptors.

In summary, the higher affinity of human nAChRs can be caused by amino acid substitutions in *α*-subunits and non-*α*-subunits. Notably, several of the potential candidates are aromatic in mouse subunits (*α*W187, *α*F189 and *ε*Y115). *β*-subunits are not a component of the ligand-binding sites, but they affect the conformation of the receptors. Sequence alignment of mouse and human *β*-subunits shows that there are 25 residue differences between mouse and human in the ECD. However, the contribution of these amino acids to nAChRs affinity is still unclear. To discover how these amino acids affect the affinity, electrophysiological recordings of site-directed mutant nAChRs need to be performed. Such experiments would allow a targeted screening of amino acids, which contribute to the different affinities between mouse and human nAChRs.

5.5 Functional diversity of the nAChR family

Among various receptors, the nAChRs family is particularly noticeable. In this greatly expanded superfamily, presently including 17 subgroups in the vertebrates (Liebeskind et al., 2015), there is no overlapping functional property for all members (Dani and Bertrand, 2007; Elgoyhen and Katz, 2012). Sequence analyses of various LGIC subunits show that the nAChR subunits are conserved to a less degree than the subunits of other LGICs (Figure 18). It has been suggested that their greater divergence in coding sequences could be the reason for the remarkable functional variety among the nAChR subunits (Marcovich et al., 2019). Roux and his colleagues (2017) reported that the diversity in the subunits sequences is the result of genome multiplications during its evolutionary history (Roux et al., 2017). Moreover, members of the nAChRs family show variable subunit stoichiometries, which can shape different functions (Nemecz et al., 2016).

It is important to understand how the variations in the structure affect nAChRs functional diversity in different species. One direct evidence came from *α*9*α*10 nAChRs in inner ear hair cells, as a unique type of proteins with highest calcium selectivity. It was found that whenever a rat *α*9 subunit is present, calcium permeability of the receptors is high; on the other hand, whenever a chicken *α*9 subunit is present, the calcium permeability of the receptors is low. Moreover, the substitution of mammalian *α*9 into chicken *α*9*α*10 nAChRs produced a lower calcium

permeability than the mammalian receptors. This calcium permeability is related to the hair cell hyperpolarization, which is suggested as an evolutionary consequence for enhancing high-frequency hearing in mammals (Lipovsek et al., 2012, 2014). Another example of the structure-function relationship is $\alpha 4\beta 2$ nAChRs in the human brain, as a main target for nicotine addiction. This subtype can be assembled by two stoichiometries, which have different physiological properties: $(\alpha 4)_2(\beta 2)_3$ and $(\alpha 4)_3(\beta 2)_2$. Depending on the nicotine amount, $\alpha 4\beta 2$ nAChRs shift between these two assemblies. The $(\alpha 4)_2(\beta 2)_3$ receptors have a higher nicotine affinity than the $(\alpha 4)_3(\beta 2)_2$ receptors (Nelson et al., 2003). All these observations confirm the conclusion of this study, that muscle type nAChRs can have different function characteristics among various species.

6 References

Akabas MH, Karlin A (1995) Identification of acetylcholine receptor channel-lining residues in the M1 segment of the *α*-subunit. *Biochemistry*. 34, 12496–12500.

Akk G, Auerbach A (1996) Inorganic, monovalent cations compete with agonists for the transmitter binding site of nicotinic acetylcholine receptors. *Biophys J*. 70, 2652–2658.

Albuquerque EX, Pereira EF, Alkondon M, Rogers SW (2009) Mammalian Nicotinic Acetylcholine Receptors: From Structure to Function. *Physiol Rev*. 89, 73–120.

Askanas V, Kwan H, Alvarez RB, Engel WK, Kobayashi T, Martinuzzi A, Hawkins EF (1987) De novo neuromuscular junction formation on human muscle fibres cultured in monolayer and innervated by foetal rat spinal cord: Ultrastructural and ultrastructural-cytochemical studies. *J Neurocytol.* 16, 523–537.

Arias HR (2000) Localization of agonist and competitive antagonist binding sites on nicotinic acetylcholine receptors. *Neurochem Int*. 36, 595–645.

Auerbach A, Akk G (1998) Desensitization of mouse nicotinic acetylcholine receptor channels. A two-gate mechanism. *J Gen Physiol*. 112, 181–197.

Auerbach A, Linglet C (1987) Activation of the primary kinetic modes of large- and small-conductance cholinergic ion channels in Xenopus myocytes. *J Physiol*. 393, 437–466.

Ausubel F, Brent R, Kingston R, Moore D, Seidman J, Smith J, Struhl K (1992) Short Protocols in Molecular Biology. John Wiley & Sons, Inc., New York.

Barchan D, Kachalsky S, Neumann D, Vogelt Z, Ovadiat M, Kochvat E, Fuchs S (1992) How the mongoose can fight the snake: the binding site of the mongoose acetylcholine receptor. *Proc Natl Acad Sci U S A*. 89, 7717–7721.

Barchan D, Ovadia M, Kochva E, Fuchs S (1995) The binding site of the nicotinic acetylcholine receptor in animal species resistant to α-bungarotoxin. *Biochemistry*. 34, 9172–9176.

Blount P, Merlie JP (1989) Molecular basis of the two nonequivalent ligand binding sites of the muscle nicotinic acetylcholine receptor. *Neuron*. 3, 349–357.

Bouzat C, Barrantes F, Sine S (2000) Nicotinic receptor fourth transmembrane domain: hydrogen bonding by conserved threonine contributes to channel gating kinetics. *J Gen Physiol*. 115, 663–672.

Brejc K, van Dijk WJ, Klaassen RV, Schuurmans M, van Der Oost J, Smit AB, Sixma TK (2001) Crystal structure of an ACh-binding protein reveals the ligand-binding domain of nicotinic receptors. *Nature*. 411, 269–276.

Brett RS, Dilger JP, Adams PR, Lancaster B (1986) A method for the rapid exchange of solutions bathing excised membrane patches. *Biophys J*. 50, 987–992.

Cadugan DJ, Auerbach A (2007) Conformational dynamics of the alphaM3 transmembrane helix during acetylcholine receptor channel gating. *Biophys J*. 93, 859–865.

Changeux JP, Bertrand D, Corringer PJ, Dehaene S, Edelstein S, Léna C, Le Novère N, Marubio L, Picciotto M, Zoli M (1998) Brain nicotinic receptors: structure and regulation, role in learning and reinforcement. *Brain Res Rev*. 26, 198–216.

Changeux JP, Taly A (2008) Nicotinic receptors, allosteric proteins and medicine. *Trends Mol Med*. 14, 93–102.

Chen J, Zhang Y, Akk G, Sine S, Auerbach A (1995) Activation kinetics of recombinant mouse nicotinic acetylcholine receptors: mutations of alpha-subunit tyrosine 190 affect both binding and gating. *Biophys J*. 69, 849–859.

Chenna R, Sugawara H, Koike T, Lopez R, Gibson TJ, Higgins DG, Thompson JD (2003) Multiple sequence alignment with the Clustal series of programs. *Nucleic Acids Res*. 31, 3497–3500.

Colquhoun D, Ogden D (1988) Activation of ion channels in the frog endplate by high concentrations of acetylcholine. *J Physiol*. 395, 131–159.

Colquhoun D, Sakmann B (1981) Fluctuations in the microsecond time range of the

current through single acetylcholine receptor ion channels. *Nature*. 294, 464–466.

Colquhoun D, Sakmann B (1985) Fast events in single-channel currents activated by acetylcholine and its analogues at the frog muscle end-plate. *J Physiol*. 369, 501–557.

Corringer PJ, Le Novère N, Changeux JP (2000). Nicotinic receptors at the amino acid level. *Annu Rev Pharmacol Toxicol*. 40, 431–458.

Corringer PJ, Poitevin F, Prevost MS, Sauguet L, Delarue M, Changeux JP (2012) Structure and Pharmacology of Pentameric Receptor Channels: From Bacteria to Brain. *Structure*. 20, 941–56.

Dani J, Bertrand D (2007) Nicotinic Acetylcholine Receptors and Nicotinic Cholinergic Mechanisms of the Central Nervous System. *Annu Rev Pharmacol Toxicol*. 47, 699–729.

del Castillo J, Katz B (1956) Localization of active spots within the neuromuscular junction of the frog. *J Physiol*. 132, 630–649.

del Castillo J, Katz B (1957) Interaction at end-plate receptors between different choline derivatives. *Proc R Soc Lond B Biol Sci*. 146, 369–381.

Dellisanti CD, Yao Y, Stroud JC, Wang ZZ, Chen L (2007a) Crystal structure of the extracellular domain of nAChR *α*1 bound to α-bungarotoxin at 1.94 Å resolution. *Nat Neurosci*. 10, 953–962.

Dellisanti CD, Yao Y, Stroud JC, Wang ZZ, Chen L (2007b) Structural determinants for alpha-neurotoxin sensitivity in muscle nAChR and their implications for the gating mechanism. *Channels (Austin)*. 1, 234–237.

Dudel J, Franke C, Hatt H (1990) Rapid activation, desensitization, and resensitization of synaptic channels of crayfish muscle after glutamate pulses. *Biophys J*. 57, 533–545.

Dudel J, Hallermann S, Heckmann M (2000) Quartz glass pipette puller operating with a regulated oxy-hydrogen burner. *Pflugers Arch*. 441, 175–180.

Dunant Y, Gisiger V (2017) Ultrafast and Slow Cholinergic Transmission. Different Involvement of Acetylcholinesterase Molecular Forms. *Molecules*. 22, 1300.

Eccles JC, Katz B, Kuffler SW (1942) Effect of eserine on neuromuscular transmission. *J Neurophysiol*. 5, 211–230.

Edelstein SJ, Schaad O, Henry E, Bertrand D, Changeux JP (1996) A kinetic mechanism for nicotinic acetylcholine receptors based on multiple allosteric transitions. *Biol Cybern*. 75, 361–379.

Elgoyhen AB, Katz E (2012) The efferent medial olivocochlear-hair cell synapse. *J Physiol Paris*. 106, 47–56.

Engel AG, Ohno K, Milone M, Wang HL, Nakano S, Bouzat C, Pruitt JN 2nd, Hutchinson DO, Brengman JM, Bren N, Sieb JP, Sine SM (1996) New mutations in acetylcholine receptor subunit genes reveal heterogeneity in the slow-channel congenital myasthenic syndrome. *Hum Mol Genet*. 5, 1217–1227.

Fatt P, Katz B (1952) Spontaneous subthreshold potentials at motor nerve endings. *J Physiol*. 117, 109–128.

Francis PT, Palmer AM, Snape M, Wilcock GK (1999) The cholinergic hypothesis of Alzheimer's disease: a review of progress. *J Neurol Neurosurg Psychiatry*. 66, 137–147.

Franke C, Hatt H, Dudel J (1987) Liquid filament switch for ultra-fast exchanges of solutions at excised patches of synaptic membrane of crayfish muscle. *Neurosci Lett*. 77, 199–204.

Franke C, Hatt H, Dudel J (1991a) Steep concentration dependence and fast desensitization of nicotinic channel currents elicited by acetylcholine pulses, studied in adult vertebrate muscle. *Pflugers Arch*. 417, 509–516.

Franke C, Hatt H, Parnas H, Dudel J (1991b) Kinetic constants of the acetylcholine (ACh) receptor reaction deduced from the rise in open probability after steps in ACh concentration. *Biophys J*. 60, 1008–1016.

Franklin GI, Yasin R, Hughes BP, Thompson EJ (1980) Acetylcholine receptors in cultured human muscle cells. *J Neurol Sci.* 47, 317–327.

Galzi JL, Changeux JP (1994) Neurotransmitter-gated ion channels as unconventional allosteric proteins. *Curr Opin Struct Biol.* 4, 554–565.

Garcia-Borron JC, Chinchetru MA, Martinez-Carrion M (1990) Selective labeling of alpha-bungarotoxin with fluorescein isothiocyanate and its use for the study of toxin-acetylcholine receptor interactions. *J Protein Chem*. 9, 683–93.

Gentile LN, Basus VJ, Shi QL, Hawrot E (1995) Preliminary two-dimensional $^{[1H]}$NMR characterization of the complex formed between an 18-amino acid peptide fragment of the alpha-subunit of the nicotinic acetylcholine receptor and alpha-bungarotoxin. *Ann N Y Acad Sci*. 757, 222–237.

Goodsell DS (2009) Neuromuscular synapse. *Biochem Mol Biol Educ*. 37, 204–210.

Griesmann GE, McCormick DJ, De Aizpurua HJ, Lennon VA (1990) Alpha-bungarotoxin binds to human acetylcholine receptor alpha-subunit peptide 185-199 in solution and solid phase but not to peptides 125-147 and 389-409. *J Neurochem*. 4, 1541–1547.

Hallermann S, Heckmann S, Dudel J, Heckmann M (2005) Short openings in high resolution single channel recordings of mouse nicotinic receptors. *J Physiol*. 563, 645–662.

Hamill O, Marty A, Neher E, Sakmann B, Sigworth F (1981) Improved patch-clamp techniques for high-resolution current recording from cells and cell-free membrane patches. *Pflugers Arch*. 391, 85–100.

Heckmann M, Bufler J, Franke C, Dudel J (1996) Kinetics of Homomeric GluR6 Glutamate Receptor Channels. *J Biophys*. 71, 1743–1750.

Heckmann M, Pawlu C (2002) Patch-Clamp Analysis - Chapter 7: Fast-Drug Application. Boulton A, Baker G (eds). Human Press, Inc., New Jersey.

Hille B (2007) Ion channels of excitable membranes, Chapter 7: Modulation, slow synaptic action, and second messengers. 3rd. ed., Sinauer: Sunderland, Mass.

Himmelheber AM, Sarter M, Bruno JP (2000) Increases in cortical acetylcholine release during sustained attention performance in rats. *Brain Res Cogn Brain Res*. 9, 313–125.

Hodgkin AL, Huxley AF, Katz B (1949) Ionic currents underlying activity in the giant axon of the squid. *Arch Sci physiol*. 3,129–150.

Hucho F, Tsetlin V, Machold J (1996) The emerging three-dimensional structure of a receptor. The nicotinic acetylcholine receptor. *Eur J Biochem*. 239, 539–557.

Ishikawa Y, Kano M, Tamiya N, Shimada Y (1985) Acetylcholine receptors of human skeletal muscle: a species difference detected by snake neurotoxins. *Brain Res*. 346, 82–88.

Ishikawa Y, Menez A, Hori H, Yoshida H, Tamiya N (1977) Structure of snake toxins and their affinity to the acetylcholine receptor of fish electric organ. *Toxicon*. 15, 477–488.

Kachalsky S, Jensen B, Barchan D, Fuchs S (1995) Two subsites in the binding domain of the acetylcholine receptor: an aromatic subsite and a proline subsite. *Proc Natl Acad Sci U S A*. 92, 10801–10805.

Kandel ER, Schwartz JH, Jessell TM (2000) Principles of neural science, Chapter 12: Synaptic integration. 4th ed., McGraw-Hill: New York.

Kao PN, Karlin A (1986) Acetylcholine receptor binding site contains a disulfide cross-link between adjacent half-cystinyl residues. *J Biol Chem*. 261, 8085–8088.

Karlin A (1967) On the application of “a plausible model” of allosteric proteins to the receptor for acetylcholine. *J Theor Biol*. 16, 306–320.

Karlin A (1993) Structure of nicotinic acetylcholine receptors. *Curr Opin Neurobiol*. 3, 299–309.

Karlin A (2002) Emerging structure of the nicotinic acetylcholine receptors. *Nat Rev Neurosci*. 3, 102–114.

Karlin A, Akabas M (1995) Toward a structural basis for the function of nicotinic acetylcholine receptors and their cousins. *Neuron*. 15, 1231–1244.

Karlin A, Holtzman E, Yodh N, Lobel P, Wall J, Hainfeld J (1983) The arrangement of the subunits of the acetylcholine receptor of Torpedo californica. *J Biol Chem*. 258, 6678–681.

Katz B, Miledi R (1970) Membrane noise produced by acetylcholine. *Nature*. 226, 962–963.

Katz B, Miledi R (1971) Further observations on acetylcholine noise. *Nat New Biol*. 232, 124–126.

Katz B, Miledi R (1973a) The binding of acetylcholine to receptors and its removal from the synaptic cleft. *J Physiol*. 231, 549–574.

Katz B, Miledi R (1973b) The effect of α-bungarotoxin on acetylcholine receptors. *Br J Pharmacol*. 49, 138–139.

Kemp DS (1995) How to promote proton transfer. *Nature*. 373, 196–197.

Keller SH, Kreienkamp HJ, Kawanishi C, Taylor P (1995) Molecular determinants conferring alpha-toxin resistance in recombinant DNA-derived acetylcholine receptors, *J Biol Chem*. 270, 4165–4171.

Kreienkamp HJ, Sine SM, Maeda RK, Taylor P (1994) Glycosylation sites selectively interfere with alpha-toxin binding to the nicotinic acetylcholine receptor. *J Biol Chem*. 269, 8108–8114.

Komiyama NH, Miyazaki G, Tame J, Nagai K (1995) Transplanting a unique allosteric effect from crocodile into human haemoglobin. *Nature*. 373, 244–246.

Kuffler SW and Yoshikami D (1975) The number of transmitter molecules in a quantum: An estimate from iontophoretic application of acetylcholine at the neuromuscular synapse. *J Physiol*. 251, 465–482.

Labarca P, Montal MS, Lindstrom JM, Montal M (1985) The occurrence of long openings in the purified cholinergic receptor channel increases with acetylcholine concentration. *J Neurosci*. 5, 3409–3413.

Lape R, Colquhoun D, Sivilotti LG (2008) On the nature of partial agonism in the nicotinic receptor superfamily. *Nature*. 454, 722–727.

Lape R, Krashia P, Colquhoun D, Sivilotti LG (2009) Agonist and blocking actions of choline and tetramethylammonium on human muscle acetylcholine receptors. *J Physiol*. 587, 5045–5072.

Le Novère N, Changeux JP (1995) Molecular evolution of the nicotinic acetylcholine receptor: an example of multigene family in excitable cells. *J Mol Evol*. 40, 155–172.

Le Novère N, Corringer PJ, Changeux JP (2002) The diversity of subunit composition in nAChRs: evolutionary origins, physiologic and pharmacologic consequences. *J Neurobiol*. 53, 447–456.

Liebeskind B, Hillis D, Zakon H (2015) Convergence of ion channel genome content in early animal evolution. *Proc Natl Acad Sci U S A*. 112, E846–E851.

Lipovsek M, Im GJ, Franchini LF, Pisciottano F, Katz E, Fuchs PA, Elgoyhen AB (2012) Phylogenetic differences in calcium permeability of the auditory hair cell cholinergic nicotinic receptor. *Proc Natl Acad Sci USA*. 109, 4308–4313.

Lipovsek M, Fierro A, Pérez EG, Boffi JC, Millar NS, Fuchs PA, Katz E, Elgoyhen AB (2014) Tracking the molecular evolution of calcium permeability in a nicotinic acetylcholine receptor. *Mol Biol Evol*. 31, 3250–3265.

Liu Y, Dilger JP (1991) Opening rate of acetylcholine receptor channels. *Biophys J*. 60, 424–432.

Love RA, Stroud RM (1986) The crystal structure of alpha-bungarotoxin at 2.5 A resolution: relation to solution structure and binding to acetylcholine receptor. *Protein Eng*. 1, 37–46.

Maconochie DJ, Knight DE (1989) A method for making solution changes in the sub-

millisecond range at the tip of a patch pipette. *Pflugers Arch*. 414, 589–596.

Marcovich I, Moglie M, Freixas A, Trigila A, Franchini L, Plazas P, Lipovsek M, Elgoyhen A (2019) Distinct evolutionary trajectories of neuronal and hair cell nicotinic acetylcholine receptors. doi: 10.1101/621342.

Matthews-Bellinger J, Salpeter MM (1978) Distribution of acetylcholine receptors at frog neuromuscular junctions with a discussion of some physiological implications. *J Physiol*. 279, 197–213.

Mishina M, Takai T, Imoto K, Noda M, Takahashi T, Numa S, Methfessel C, Sakmann B (1986) Molecular distinction between fetal and adult forms of muscle acetylcholine receptor. *Nature*. 321, 406-411.

Mishina M, Tobimatsu T, Imoto K, Tanaka K, Fujita Y, Fukuda K, et al. (1985) Location of functional regions of acetylcholine receptor alpha-subunit by site-directed mutagenesis. *Nature*. 313, 364–369.

Miyazawa A, Fujiyoshi Y, Unwin N (2003) Structure and gating mechanism of the acetylcholine receptor pore. *Nature*. 423, 949–955.

Nagwaney S, Harlow ML, Jung JH, Szule JA, Ress D, Xu J, Marshall RM, McMahan UJ (2009) Macromolecular connections of active zone material to docked synaptic vesicles and presynaptic membrane at neuromuscular junctions of mouse. *J Comp Neurol*. 513, 457–68.

Nayak TK, Chakraborty S, Zheng W, Auerbach A (2016) Structural correlates of affinity in fetal versus adult endplate nicotinic receptors. *Nat Commun*. 7, 11352.

Neher E, Sakmann B (1976) Single-channel currents recorded from membrane of denervated frog muscle fibres. *Nature*. 260, 799–802.

Nelson ME, Kuryatov A, Choi CH, Zhou Y, Lindstrom J (2003) Alternate stoichiometries of alpha4beta2 nicotinic acetylcholine receptors. *Mol Pharmacol*. 63, 332–341.

Nemecz Á, Prevost MS, Menny A, Corringer PJ (2016) Emerging Molecular

Mechanisms of Signal Transduction in Pentameric Ligand-Gated Ion Channels. *Neuron*. 90, 452–470.

Neumann D, Barchan D, Horowitz M, Kochva E, Fuchs S (1989) Snake acetylcholine receptor: cloning of the domain containing the four extracellular cysteines of the alpha subunit. *Proc Natl Acad Sci U S A*. 86, 7255–7259.

Nicholls JG, Martin AR, Wallace BG, Fuchs PA (2000) From Neuron to Brain. 4th ed., Sunderland: Sinauer Associates, Inc.

Ogden D, Colquhoun D (1985) Ion channel block by acetylcholine, carbachol and suberyldicholine at the frog neuromuscular junction. *Proc R Soc L B Biol Sci*. 225, 329–355.

Ohno K, Wang H-L, Milone M, Bren N, Brengman JM, Nakano S, Quiram P, Pruitt JN, Sine SM, Engel AG (1996) Congenital myasthenic syndrome caused by decreased agonist binding affinity due to a mutation in the acetylcholine receptor *ε* subunit. *Neuron*. 17, 157–170.

O'Leary ME, White MM (1992) Mutational analysis of ligand-induced activation of the Torpedo acetylcholine receptor. *J Biol Chem*. 267, 8360–8365.

Ortells MO, Lunt GG (1995) Evolutionary history of the ligand-gated ion-channel superfamily of receptors. *Trends Neurosci*. 18, 121–127.

Parzefall F, Wilhelm R, Heckmann M, Dudel J (1998) Single channel currents at six microsecond resolution elicited by acetylcholine in mouse myoballs. *J Physiol*. 512, 181–188.

Pawlu C, DiAntonio A, Heckmann M (2004) Postfusional control of quantal current shape. *Neuron*. 42, 607–618.

Pedersen JE, Bergqvist CA, Larhammar D (2019) Evolution of vertebrate nicotinic acetylcholine receptors. *BMC Evol Biol*. 19, 38.

Prinston JE, Emlaw JR, Dextraze MF, Tessier CJG, Pérez-Areales FJ, McNulty MS, daCosta CJB (2017) Ancestral Reconstruction Approach to Acetylcholine Receptor

Structure and Function. *Structure*. 25, 1295–1302.

Ranawaka UK, David G. Lalloo DG, de Silva HJ (2013) Neurotoxicity in snakebite – the limits of our knowledge. *PLoS Negl Trop Dis*. 7, e2302.

Ridley RM, Bowes PM, Baker HF, Crow TJ (1984) An involvement of acetylcholine in object discrimination learning and memory in the marmoset. *Neuropsychologia*. 22, 253–263.

Roux J, Liu J, Robinson-Rechavi M (2017) Selective constraints on coding sequences of nervous system genes are a major determinant of duplicate gene retention in vertebrates. *Mol Biol Evol*. 34, 2773–2791.

Salamone FN, Zhou M, Auerbach A (1999) A re-examination of adult mouse nicotinic acetylcholine receptor channel activation kinetics. *J Physiol*. 516, 315–330.

Salpeter MM, Smith CD, Matthews-Bellinger JA (1984) Acetylcholine receptor at neuromuscular junctions by EM autoradiography using mask analysis and linear sources. *J Electron Microsc Tech*. 1, 63–81.

Silva A, Hodgson WC, Geoffrey K. Isbister GK (2017) Antivenom for neuromuscular paralysis resulting from snake envenoming.*Toxins (Basel)*. 9, 143.

Sine SM (2002) The nicotinic receptor ligand binding domain. *J Neurobiol*. 53, 431–446.

Sine SM (2012) End-plate acetylcholine receptor: structure, mechanism, pharmacology, and disease. *Physiol Rev*. 92, 1189–1234.

Sine SM, Engel AG (2006) Recent advances in Cys-loop receptor structure and function. *Nature*. 440, 448–455.

Sine SM, Ohno K, Bouzat C, Auerbach A, Milone M, Pruitt JN, Engel AG (1995) Mutation of the acetylcholine receptor alpha subunit causes a slow-channel myasthenic syndrome by enhancing agonist binding affinity. *Neuron*. 15, 229–239.

Sine SM, Steinbach JH (1984) Agonists block currents through acetylcholine receptor channels. *J Biophys*. 46, 277–283.

Sine SM, Steinbach JH (1986a) Activation of acetylcholine receptors on clonal mammalian BC3H-1 cells by low concentrations of agonist. *J Physiol*. 373, 129–162.

Sine SM, Steinbach JH (1986b) Acetylcholine receptor activation by a site-selective ligand: nature of brief open and closed states in BC3H-1 cells. *J Physiol*. 370, 357–379.

Sine SM, Steinbach JH (1987) Activation of acetylcholine receptors on clonal mammalian BC3H-1 cells by high concentrations of agonist. *J Physiol*. 385, 325–359.

Sine SM, Taylor P (1981) Relationship between reversible antagonist occupancy and the functional capacity of the acetylcholine receptor. *J Biol Chem*. 256, 6692–6699.

Slater CR (2008) Structural factors influencing the efficacy of neuromuscular transmission. *Ann N Y Acad Sci*. 1132, 1–12.

Spura A, Russin TS, Freedman ND, Grant M, McLaughlin JT, Hawrot E (1999) Probing the agonist domain of the nicotinic acetylcholine receptor by cysteine scanning mutagenesis reveals residues in proximity to the alpha-bungarotoxin binding site. *Biochemistry*. 38, 4912–4921.

Stiles JR, Bartol TM, Salpeter MM, Salpeter EE, Sejnowski TJ (2001) Synapses - Chapter 15: Synaptic variability. Cowan WM, Südhof TC, Stevens CF (eds). Johns Hopkins University Press, Baltimore, Maryland.

Stiles JR, Van Helden D, Bartol TM Jr, Salpeter EE, Salpeter MM (1996) Miniature endplate current rise times less than 100 microseconds from improved dual recordings can be modeled with passive acetylcholine diffusion from a synaptic vesicle. *Proc Natl Acad Sci U S A*. 93, 5747–5752.

Stock P, Ljaschenko D, Heckmann M, Dudel J (2014) Agonists binding nicotinic receptors elicit specific channel-opening patterns at αγ and αδ sites. *J Physiol*. 592, 2501–2517.

Suchnya T, Xu L, Gao F, Fourtner C, Nicholson B (1993) Identification of a proline residue as a transduction element involved in voltage gating of gap junctions. *Nature (Lond.)*. 365, 847–849.

Tsunoyama K, Gojobori T (1998) Evolution of nicotinic acetylcholine receptor subunits. *Mol Biol Evol*. 15, 518–527.

Numa S, Noda M, Takahashi H, Tanabe T, Toyosato M, Furutani Y, Kikyotani S (1983) Molecular structure of the nicotinic acetylcholine receptor. *Cold Spring Harb Symp Quant Biol*. 48, 57–69.

Unwin N (1995) Acetylcholine receptor channel imaged in the open state. *Nature*. 373, 37–43.

Unwin N (2005) Refined structure of the nicotinic acetylcholine receptor at 4 Å resolution. *J Mol Biol*. 346, 967–989.

Unwin N, Fujiyoshi Y (2012) Gating movement of acetylcholine receptor caught by plunge-freezing. *J Mol Biol*. 422, 617–634.

Unwin N, Miyazawa A, Li J, Fujiyoshi Y (2002) Activation of the nicotinic acetylcholine receptor involves a switch in conformation of the alpha subunits. *J Mol Biol*. 319, 1165–1176.

Vincent A, Jacobson L, Curran L (1998) Alpha-Bungarotoxin binding to human muscle acetylcholine receptor: measurement of affinity, delineation of AChR subunit residues crucial to binding, and protection of AChR function by synthetic peptides. *Neurochem Int*. 32, 427–433.

von Beckerath N, Adelsberger H, Parzefall F, Franke C, and Dudel J (1995) GABAergic inhibition of crayfish deep extensor abdominal muscle exhibits a steep dose-response relationship and a high degree of cooperativity. *Pflugers Arch*. 429, 781–788.

Wang HL, Auerbach A, Bren N, Ohno K, Engel AG, Sine SM (1997) Mutation in the M1 domain of the acetylcholine receptor alpha subunit decreases the rate of agonist dissociation. *J Gen Physiol*. 109, 757–766.

Wilson PT, Hawrot E, Lentz TL (1988) Distribution of alpha-bungarotoxin binding sites over residues 173-204 of the alpha subunit of the acetylcholine receptor. *Mol Pharmacol*. 34, 643–650.

Young HS, Herbette LG, Skita V (2003) α-bungarotoxin binding to acetylcholine receptor membranes studied by low angle X-ray diffraction. *Biophys J*. 85, 943–953.

Zeng H, Moise L, Grant MA, Hawrot E (2001) The solution structure of the complex formed between alpha-bungarotoxin and an 18-mer cognate peptide derived from the alpha 1 subunit of the nicotinic acetylcholine receptor from *Torpedo californica*. *J Biol Chem*. 276, 22930–22940.

Zhang Y, Chen J, Auerbach A (1995) Activation of recombinant mouse acetylcholine receptors by acetylcholine, carbamylcholine and tetramethylammonium. *J Physiol*. 486, 189–206.

7 Abbreviations

α	closing rate constant
α-Bgtx	α-bungarotoxin
ACh	acetylcholine
AChE	acetylcholinesterase
AP	action potential
AZs	active zones
β	opening rate constant
DIC	differential interference contrast
ECD	extracellular domain
EPP	end-plate potential
EPSP	excitatory postsynaptic potential
HEK293T	human embryonic kidney cell-line 293T
I	mean current
$\hat{\imath}$	normalized I value
ICD	intracellular domain
LGICs	ligand-gated ion channels
JFs	junctional folds
k_{+1}, k_{+2}	association rate constant
k_{-1}, k_{-2}	dissociation rate constant
K_{50}	half-maximal responses
LBD	ligand-binding domain
$M_{\alpha}H_{\beta\delta\varepsilon}$	chimeric receptors composed of mouse α-subunits and human β-, δ- and ε-subunits
mEPCs	miniature endplate currents
mEPP	miniature end-plate potential
nA	nanoampere
nAChRs	nicotinic acetylcholine receptors
NMJ	neuromuscular junction
ODEs	ordinary differential equations
pA	picoampere
RMS	root mean square
s.e.m.	standard error of the mean

SVs	synaptic vesicles
TMD	transmembrane domain
t_r	rise-time
UniProt	Universal Protein Resource

8 Figures

9 Acknowledgements

First of all, I thank Prof. Dr. med. Manfred Heckmann, who gave me the chance to explore the field of neuroscience and supported me strongly in every aspect during my PhD research. He not only taught me electrophysiology personally, but also gave many inspiring suggestions and always encouraged me to put forward my own opinions for the studies. His thoughtful guidance has made me a better scientist.

I thank Prof. Dr. med. Josef Dudel. At several points of time during the studies, he gave his advices about nAChRs properties, which helped me stay on the track during my research.

My special thank goes to Dmitrij Ljaschenko, who performed the single-channel recordings. He helped me solve problems in my experiments and helped me understand theoretical points about channel kinetics, as well as shared with me his research experiences.

I thank Prof. Dr. med. Anna-Leena Sirén, who supported me and inspired me through my time as a PhD student.

I want to thank Achmed Mrestani, Dr. Martin Pauli, Dr. Christiane Albert-Weissenberger, Lydia Kurzinger, Katharina Lichter and Dr. Matthias Pawlak. My colleagues were always there for me and gave me a hand whenever I needed support. I also thank all other employees of Physiological Institute for their support through these years.

At last, I would like to thank my parents, who have supported me in every way they could during my studies in Germany.

10 List of publications

Yunzhi Lu, Manfred Heckmann (2019) Higher affinity of human compared to mouse nicotinic acetylcholine receptor channels. (in preparation)

Yunzhi Lu, Ying Xu, Enzhuo Yang, Chao Wang, Honghai Wang, Hongbo Shen (2012) Novel recombinant BCG coexpressing Ag85B, ESAT-6 and Rv2608 elicits significantly enhanced cellular immune and antibody responses in C57BL/6 mice. *Scand J Immunol*. 76, 271–277.

Yan Min, Wenxi Xu, Dan Liu, Suqin Shen, **Yunzhi Lu**, Lu Zhang, Honghai Wang (2010) Autophagy promotes BCG-induced maturation of human dendritic cells. *Acta Biochim Biophys Sin*. 42, 177–182.